UNIVERSITY OF CALIFORNIA SAN DIEGO

Toward Ultracold Strontium on Nanophotonics

A thesis submitted in partial satisfaction of the
requirements for the degree
Master of Science

in

Electrical Engineering (Signal and Image Processing)

by

Grady Kestler

Committee in charge:

Professor Julio Barreiro Guerrero, Chair
Professor Shayan Mookherjea, Co-Chair
Professor Fred Harris
Professor Ramesh Rao

2019

The thesis of Grady Kestler is approved, and it is acceptable in quality and form for publication on microfilm:

_____

_____

_____
Co-Chair

_____
Chair

University of California San Diego

2019

TABLE OF CONTENTS

LIST OF FIGURES

LIST OF TABLES

VITA

2014	B. S. in Music/Interdisciplinary Computing and the Arts, University of California San Diego
2017	M. F. A. in Theater (Sound Design), University of California San Diego
2019	(Expected) M. S. in Electrical Engineering (Signal and Image Processing), University of California San Diego

PUBLICATIONS

Grady Kestler, Shahrokh Yadegari, and David Nahamoo. "Head Related Impulse Response Interpolation and Extrapolation Using Deep Belief Networks." *ICASSP 2019-2019 IEEE International Conference on Acoustics, Speech and Signal Processing (ICASSP)*. IEEE, 2019.

Steven Leffue, Grady Kestler, "AIIS: An Intelligent Improvisation System", *International Computer Music Conference*, 314, 2016.

ABSTRACT OF THE THESIS

Toward Ultracold Strontium on Nanophotonics

by

Grady Kestler
Master of Science in Electrical Engineering (Signal and Image Processing)

University of California San Diego, 2019

Professor Julio Barreiro Guerrero, Chair
Professor Shayan Mookherjea, Co-Chair

Using matter wave interferometry to perform high precision measurements is an exciting field of modern day physics and engineering. Physical constants and anomalies too small to observe with classical devices can be probed and measured with quantum technology. The ability to control the wave nature of a specific particle opens up a vast set of methodologies engineered for the given particle. The most complete toolboxes exist for alkali metals such as rubidium and cesium. The atomic structure of strontium provides a number of advantages in further developing these methods and technologies, especially in the resolution of spectroscopic measurements.

A promising method of matter-wave control utilizes optical waveguides and atomic properties to trap and guide matter waves. Using laser cooling techniques, atoms are cooled to microkelvin temperatures before being loaded onto the nanophotonic chip, thus receiving the appropriate name, atom-on-chip devices. The ability to manufacture the photonic waveguides in a multitude of different arrangements shows promise in being able to develop atomtronic devices which are equivalent to electronic devices, but utilize matter-waves of neutral atoms instead

of electrons.

The heart of our novel technology is an ultra-high vacuum (UHV) apparatus with sample loading capabilities. In this thesis, I discuss the design and construction of the apparatus to provide quick turn over between loading nanophotonic devices and experimental trapping by separation of the main chamber from a load lock. The ultimate pressures in both reach 3.8×10^{-11} and below 1×10^{-11} Torr and initial trials were conducted with a 36-48 hour turn over between loading a chip at atmosphere, and inserting it into the UHV main chamber. These metrics beats other groups by an order of magnitude in pressure and others week-long loading time. Continual improvements are being made to further decrease this time.

Chapter 1

Introduction

Ultracold trapping of neutral atoms has been a fruitful field in understanding fundamental physics and developing new technologies. Quantum emulation which simulates quantum mechanics of many body systems, is one such example that has benefited significantly from the field by utilizing many particle systems to probe fundamental interactions [4]. In a similar vein, atom-photon interactions for quantum networks and quantum memories of light have also been explored extensively in the context of quantum information and quantum metrology [11, 19, 20]. Interfacing between neutral atoms and nanophotonic chips in atom-on-chip systems has been constructive with one such system having recently been installed on the International Space Station [8]. Other atom-on-chip experiments probe fundamental physics of Johnson noise [7, 10] and surface interactions [6, 10, 17, 18] near the boundary of the cold atoms and chip surfaces.

Current experiments of this sort revolve around a single species of atom, the choice of which defines a majority of the subsequent design and equipment decisions. Rubidium, cesium, and ytterbium are common choices due to their ease of cooling on the wide, single valence transitions. Strontium, on the other hand, is an alkali earth metal with two valence electrons. It has become a more recent

interest of ultracold atomic experiments [1, 25] due to its multiple stage cooling and stable transitions which worked in combination to measured the most accurate atomic clock [12].

Despite the atomic species of choice, the heart of all ultracold experiments is the ultra-high vacuum chamber reaching pressures on the order of 1×10^{-11} Torr. As is expected, in order to add components like nanophotonic chips and other surface elements on which the atomic gases are trapped and probed, the chamber must be brought to atmospheric pressures and re-pumped to ultra-high vacuum levels often. The larger the chamber, the longer the re-pumping process. One solution is to separate a smaller portion of the apparatus to designate as a load-lock. Through an ultra-high vacuum valve, only the small volume load-lock is exposed to atmosphere while the chip is loaded. The main chamber remains at UHV while the load-lock is sealed and re-pumped. The smaller volume pumps faster and the chip can be loaded into a UHV chamber within 24 to 36 hours after loading.

The design and construction of such an apparatus is the main contribution of this thesis. Chapter 2 discusses the theory of atomic cooling and trapping, while the atomic nature of strontium is covered in Chapter 3. Furthermore, Chapter 4 details the design consideration and procedures followed in construction of the apparatus and ultimately reaching ultra-high vacuum. Finally, Chapter 5 illustrates the plan for future work of this apparatus including measurement of the Casimir-Polder potential and trapping strontium on an optical nanofiber.

Chapter 2

Cooling and Trapping Atoms

Here, I discuss the different stages in atomic cooling. In order to cool and trap ^{88}Sr, the isotope used in our experiments, only two stages are necessary; Doppler cooling and a Magneto-Optical Trap (MOT). Furthermore, we also employ far off resonant traps (FORTs) to control the ^{88}Sr near nanophotonic surfaces. The theory behind these three topics is discussed in this chapter.

2.1 Doppler Cooling

Because atomic thermal energy is proportional to its motion, cooling and slowing an atomic beam are equivalent. The easiest means of decelerating the atomic beam is to apply a force in the opposite direction of propagation by employing the radiative forces of light. As shown in [2], this force can be described as

$$F_{scattering} = (\text{photon absorption}) \times (\text{scattering rate})$$

The scattering rate is considered to be $\Gamma\rho_{22}$ where Γ is the two level transition linewidth and ρ_{22} is the fraction of atoms in the excited state. This yields a force

$$F_{scattering} = \hbar k \frac{\Gamma}{2} \frac{\frac{I}{I_{sat}}}{1 + \frac{I}{I_{sat}} + 4\frac{\delta^2}{\Gamma^2}}$$

and I is the laser intensity, I_{sat} is the saturation intensity of the transition, and $\delta = \omega - \omega_0 + kv$ is the de-tuning of the laser frequency ω from the transition

resonance ω_0 with a Doppler shift of kv. Maximizing the cooling force, $\delta = 0$ and $I \to \infty$, we find that $F_{max} = \hbar k \frac{\Gamma}{2}$ and the maximum deceleration of an atom with mass M will be

$$a_{max} = \frac{F_{max}}{M} = \frac{\hbar k \Gamma}{2M} = \frac{v_r}{2\tau}$$

The recoil velocity, $v_r = \frac{\hbar k}{M}$, is defined to be the velocity change of the atom from absorption of the photon and $\tau = \frac{1}{\Gamma}$ is the lifetime of the excited state.

The recoil of the atom also produces a transfer of heat from the photon to the atom resulting in a slight heating of the atom which sets a lower limit on the achievable temperature from Doppler cooling. This minimum temperature occurs when the heating and cooling energies of the atom are at equilibrium. The kinetic energy produced by the recoil of the atom is

$$E_r = \frac{1}{2} M v_r^2$$

while the internal thermal energy of the atom by the equipartition theorem is $\frac{1}{2} k_B T$ where k_B is the Boltzmann constant and T is the atom's temperature. Setting these equal yields our lower temperature bound of the atoms at

$$T_{Doppler} = \frac{\hbar \Gamma}{2 k_B} \tag{2.1}$$

where Γ is the natural linewidth of the transition and k_B is Boltzmann's constant.

2.2 Zeeman Slower

The initial speed of the atom $\mathbf{v}$ is so large that the photons at frequency ω_0, in the atom frame, are seen to be at a lower wavelength due to a Doppler shift; $\omega_0 - \Delta$. To compensate this affect, we de-tune the laser to a wavelength of $\omega_0 + \Delta$, known as red de-tuning since the photons are shifted away from resonance toward the red end of the spectrum. Alternatively, blue de-tuning shifts the resonant frequency towards the blue end of the spectrum. By red de-tuning the laser by the same amount that the photons are blue shifted in the atom frame, the photons will appear on resonant with the atomic transition.

As the atom velocity decreases by absorbing and emitting photons, the photons in the atom frame become un-Doppler shifted. In the lab frame, this

indicates a need to change the laser de-tuning as a function of position down the tube. To accomplish this, magnetic fields along the tube induce Zeeman shifts to counteract the change in Doppler shifts. The varying magnetic field, dubbed a Zeeman slower, tunes the strength of the magnetic field at every position to keep the atomic transitions on resonant with a fixed laser frequency.

2.3 Magneto-Optical Trap

Until now, we have only been concerned with atomic beams that are traveling in a single direction. Realistically, the atoms travel in all 3 directions and thus the Doppler cooling process is applied along 3 orthogonal axes with 2 counter-propagating, slightly red de-tuned laser beams on each axis. Additionally, we wish to apply a spatially dependent force in order to constrain the atoms locally in the experiment. A magnetic field which is zero at the trap center and non-zero away from the center, provides this additional force using spatially dependent Zeeman shifts away from the center of the trap.

In a static magnetic field, $\mathbf{B}$, we can define the interaction part of the Hamiltonian to be

$$\begin{aligned}\mathbf{H_{int}} &= -\mu \cdot \mathbf{B} \\ &= -\mu_B(g_L\mathbf{L} + g_S\mathbf{S}) \cdot \mathbf{B}\end{aligned}$$

where $\mu_B = \frac{e\hbar}{2m_e}$ is the Bohr magneton, $\mathbf{S}$, and $\mathbf{L}$ are the spin and orbital angular momentum operators respectively, and g_S and g_L are the corresponding Landé factors. If we assume the magnetic field is along the z-axis, then

$$\mathbf{H_{int}} = -\mu_B B_0(g_L L_z + g_S S_z)$$

where S_z and L_z are the spin and orbital angular momentum operators along the z-axis.

In the case of a non-zero total angular momentum, $\mathbf{J} = \mathbf{L} + \mathbf{S} \neq 0$, we can calculate the energy shifts of the atom using first order perturbation theory to find

$$\Delta E = \mu_B g_J m_J B(z) \tag{2.2}$$

which is a position dependent energy shift.

Consider an atom moving away from the trap center along the z axis in the $z > 0$ direction and the magnetic field be linear near the trap center such that $B(z) \propto z$ near $z = 0$ (Figure 2.1). Taking the Landé factor to be ≈ 1, the energy shift is negative, lowering the resonance of the transition between the $J = 0$ and $J = 1$ states (Figure 2.1) to the frequency of the red-detuning the laser field. Additionally, by the transition selection rules for a $\Delta m_J = -1$, the photon needs to be left-hand circularly polarized σ^- in order to drive the transition. The radiation pressure from the photon absorption provides a restoring force back towards $z = 0$.

In the other direction, $z < 0$, we find the Zeeman splitting for the $m_J = +1$ to be on resonance with the red de-tuned laser field and thus requires a σ^+ polarized photon to drive the transition. By combining counter propagating beams along the z-axis, with $\sigma^\pm$ polarization, a restoring force proportional to z keeps the atoms trapped in the center.

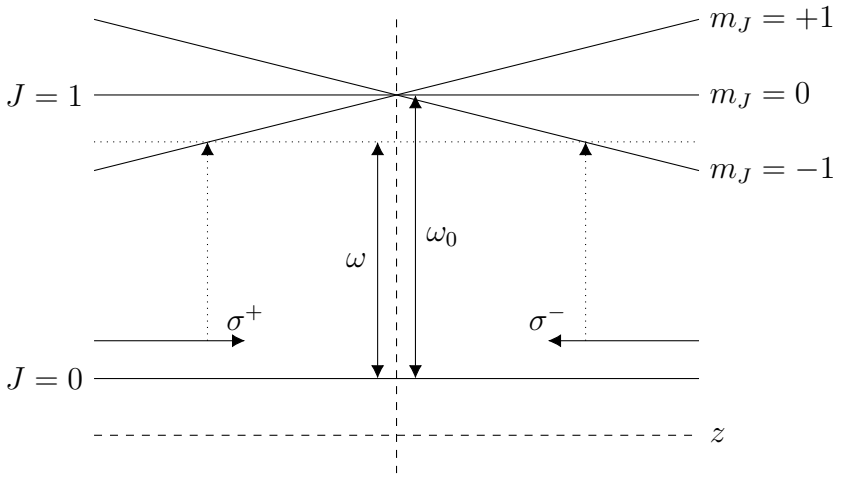

Figure 2.1: Single axis MOT cooling. A quadropole magnetic field splits the $J = 1$ state. When $z > 0$, the $m_J = -1$ becomes resonant with the σ^- polarized, red de-tuned laser field. When $z < 0$, the $m_J = +1$ becomes resonant with the σ^+, red de-tuned laser field.

Again, following the treatment in [2], we can derive the MOT force as

$$\begin{aligned} F_{MOT} &= F^{\sigma^+}_{scattering}(\omega - kv - (\omega_0 + \beta z)) + F^{\sigma^-}_{scatterint}(\omega + kv - (\omega_0 - \beta z)) \\ &= -\alpha v - \frac{\alpha\beta}{k} z \end{aligned} \tag{2.3}$$

with

$$\alpha = 4\hbar k \frac{I}{I_{sat}} \frac{-2\frac{\delta}{\Gamma}}{(1 + (\frac{2\delta}{\Gamma})^2)^2} \qquad \beta z = \frac{g\mu_B}{\hbar} \frac{dB}{dz} z$$

The first term of 2.3 provides additional cooling of the atoms and the second term provides the restoring force to confine the atoms to the trap center.

2.4 Far Off Resonant Traps

Once the atoms reach ultracold temperatures, the difficulties shift to trapping on or near a nanophotonic chip. Far off resonant traps are a result of far de-tuned laser fields interacting with a two level atom. These traps generate a force whose sign depends on whether the laser is red de-tuned or blue de-tuned providing a method for 'pushing' and 'pulling' the atoms from the surface of a photonic device.

Two Level atom in a Laser Field

Based on [24], we start with the Hamiltonian derived in Appendix B

$$\tilde{\mathbf{H}} = -\hbar\Delta \left|e\right\rangle\!\left\langle e\right| + \frac{\hbar}{2}(\Omega a + \Omega^* a^\dagger) \tag{2.4}$$

where $a = \left|g\right\rangle\!\left\langle e\right|$ and $a^\dagger = \left|e\right\rangle\!\left\langle g\right|$ are the atomic raising and lowering operators, and $\Omega = -\frac{\langle g|\hat{\epsilon}\cdot\mathbf{d}|e\rangle E_0}{\hbar}$ is the Rabi frequency. In a resonant laser field ($\Delta = 0$), we find the dynamics of the states by solving Schrodinger's equation for the probability amplitudes (c_g, c_e) of the ground and excited states.

$$\begin{aligned} c_g(t) &= c_g(0)\cos\frac{\Omega}{2}t - ic_e(0)\sin\frac{\Omega}{2}t \\ c_e(t) &= c_e(0)\cos\frac{\Omega}{2}t - ic_g(0)\sin\frac{\Omega}{2}t \end{aligned}$$

From these coupled dynamics, we can see that in the monochromatic laser field, the probability of finding the atom in the ground or excited state, oscillates with frequency $\frac{\Omega}{2}$. The Rabi frequency can also be thought of as a coupling constant between the two states in that a larger value for Ω makes it easier to transition between them while a smaller value makes it more difficult.

Given the relationship $I = 2\epsilon_0 c|E_0|^2$ where I is the laser intensity and E_0 is the magnitude of the electric field, we see that $\Omega^2 \propto I$. However, for a population of atoms initially in the ground state, increasing I does not guarantee a larger population of atoms in the excited state; as more atoms are excited, there are less atoms to absorb the resonant photons. The lifetime $\tau = \frac{1}{\Gamma}$ of the excited state dictates when the atoms return to the ground state again and thus when saturation affects begin to take place. The saturation intensity, denoted as I_{sat}, is related to the Rabi frequency by

$$2|\Omega|^2\tau^2 = \frac{2|\Omega|^2}{\Gamma^2} = \frac{I}{I_{sat}}$$

To examine the affect of a de-tuned laser, we add a kinetic energy term giving a center-of-mass Hamiltonian

$$\tilde{\mathbf{H}} = \frac{p^2}{2m} - \hbar\Delta\,|e\rangle\langle e| + \frac{\hbar}{2}(\Omega a + \Omega^* a^\dagger)$$

with dynamics

$$i\hbar\frac{\partial c_e}{\partial t} = \frac{p^2}{2m} + \frac{\hbar\Omega}{2}c_g - \hbar\Delta c_e$$
$$i\hbar\frac{\partial c_g}{\partial t} = \frac{p^2}{2m} + \frac{\hbar\Omega^*}{2}c_e$$

Here, we can make use of a few assumptions about the system to simplify the mathematics. Since the laser field is far de-tuned from resonance, if the population of atoms is initially in the ground state, then excitation will likely not occure and we can take $\frac{\partial c_e}{\partial t} = 0$ giving us a relationship between c_e and c_g.

$$(\hbar\Delta - \frac{p^2}{2m})c_e \approx \frac{\hbar\Omega}{2}c_g$$

Furthermore, the kinetic energy for ultracold atoms is much smaller than the de-tunings ($\frac{p^2}{2m} << \hbar\Delta$) and thus c_e is eliminated from the equation and

$$i\hbar\frac{\partial c_g}{\partial t} = (\frac{p^2}{2m} + \frac{\hbar|\Omega|^2}{4\Delta})c_g$$

The effective Hamiltonian that generates these dynamics is

$$H = \frac{p^2}{2m} + U_{dip}$$

where $U_{dip} = \frac{\hbar|\Omega|^2}{4\Delta}$ is the potential induced by the field on the atom. From, $\frac{2\Omega^2}{\Gamma^2} = \frac{I}{I_{sat}}$, we find the dipole force felt by the atom to be

$$U_{dip} = \frac{\hbar\Gamma^2}{8\Delta}\frac{I}{I_{sat}}$$
$$F_{dip} = -\boldsymbol{\nabla} U_{dip} = -\frac{\hbar\Gamma^2}{8\Delta I_{sat}}\boldsymbol{\nabla} I \tag{2.5}$$

Clearly the force in proportional to the sign of the laser de-tuning. For a red de-tuned laser, $\Delta = \omega - \omega_0 > 0$ gives an attractive force while a blue de-tuned laser, $\Delta < 0$ gives a repulsive force. This dipole force is often used in evaporative cooling, but in the context of atom-on-chip trapping, it more promising as a means to control the trapping distance from the chip.

AC Stark Shifts

From the Hamiltonian from Eq 2.4

$$\tilde{\mathbf{H}} = \begin{bmatrix} -\hbar\Delta & \frac{\hbar}{2}\Omega \\ \frac{\hbar}{2}\Omega^* & 0 \end{bmatrix}$$

the ground and excited states of the original atom are no longer eigenstates. We can find new energy eigenstates with energies $E_\pm = -\frac{\hbar\Delta}{2} \pm \frac{\hbar\tilde{\Omega}}{2}$ where $\tilde{\Omega} = \sqrt{|\Omega|^2 + \Delta^2}$ is the generalized Rabi frequency. The new states corresponding to these energies are called dressed states and are denoted by $|\pm\rangle$. For an atom placed in a far, red de-tuned Gassian beam, the energy shift varies based on the intensity where the ground state sees a potential well and the excited state sees an equal and opposite potential barrier (Figure 2.2). The energy shift based on the potential well is

$$-\frac{\hbar\tilde{\Omega}}{2} \approx \frac{\hbar\Delta}{2} + \frac{\hbar|\Omega|^2}{4\Delta}$$

For two level atoms, this shift is always opposite and equal for the ground and excited state, but due to more complex features of actual atomic structure, it

is possible to find de-tunings such that the ground and excited states are actually shifted equally (both in sign and magnitude) [24]. These wavelengths are called *magic* wavelengths and are important when trapping on nanophotonics.

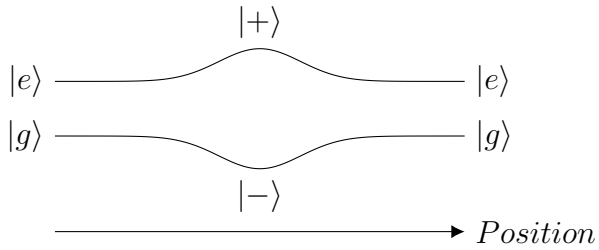

Figure 2.2: AC Stark shifts of ground and excited state of a two level atom in a red de-tuned laser field. As we vary position through the Gaussian beam, the excited and ground state shift into the dressed states, $|\pm\rangle$, at the highest intensity. In a blue de-tuned field, the shift is inverted.

The quantum mechanical derivation for the dipole force and AC Stark shifts assumes we are dealing with a two level atom. Since we are interested in cancelling the AC Stark shifts for a real atom, a more general form of the dipole potential in the rotating wave approximation is [5]

$$U_{dip} = -\frac{1}{2\epsilon_0 c} Re(\alpha) I \tag{2.6}$$

where α is the atomic polarization; a measure of how easily the atom is polarized in the electric field. Calculating the *magic* wavelengths that cancel the AC Stark shifts of two states is equivalent to finding a wavelength that results in both the ground and excited state have the same polarizability [1].

Chapter 3

Strontium

There are four stable isotopes of strontium, only one of which, ^{87}Sr, is Fermionic with a nuclear spin of $\frac{9}{2}$. Of the remaining Bosonic isotopes, ^{88}Sr, is the most abundant followed by ^{86}Sr and lastly ^{84}Sr. Each of the Bosonic species has similar electronic properties, but vary significantly in the s-wave scattering length, a; a measure of the interaction. Table 3.1 summarizes these properties of each isotope.

Table 3.1: Abundance and nuclear spin of different isotopes of strontium. s-wave scattering lengths are given in units of a_0. Values taken from [25]

Isotope	Abundance	Nuclear Spin	Like-species Scattering Length
^{84}Sr	.56%	0	124
^{86}Sr	9.86%	0	830
^{87}Sr	7.00%	9/2	97
^{88}Sr	82.58%	0	-1

The nuclear spin of the Fermionic isotope, ^{87}Sr, generates a number of challenges in cooling and trapping. There are 10 possible internal states, $\frac{9}{2}, \frac{7}{2}, ..., -\frac{7}{2}, -\frac{9}{2}$, and thus 10 states to simultaneously cool and trap. This is due to the nuclear spin interacting with the electronic spin (spin-spin coupling) generating what is known as the hyper-fine splitting of the electronic states. This makes it difficult to use ^{87}87, and any other Fermionic matter, to be employed for atom-on-chip purposes.

Of the remaining isotopes, we consider the purposes and future of this work surrounding precision metrology and the affect of scattering lengths. When trying to reach quantum degeneracy, evaporative cooling is often a final step in the process and longer scattering lengths become quite useful. This is because evaporative cooling works like shaking a cup of ping-pong balls. As the balls interact with each other, the faster moving ones are ejected from the cup leaving only the slower, colder balls. If the ping-pong balls did not interact with each other, no amount of shaking would eject the hotter balls. On the other hand, when performing matter-wave interferometry for precision measurements, we do not want the atomic populations to interact with each other. Strong interactions, in this case, will affect the interference patterns disrupting the measurement. For this work, we will be using ^{88}Sr isotope due to its small scatter length and high natural abundance.

Laser Cooling

The spherically symmetric ground state ($L = 0$) of strontium provides a series of optical transitions useful in cooling and trapping ^{88}Sr. Three of these transitions are shown in Figure 3.1 and all occur in the visible spectrum. The linewidth measurement , Γ, is related to the lifetime of the excited state, τ, by $\Gamma = \frac{1}{\tau}$. Thus a broader transition has a smaller lifetime.

The broadest transition we are concerned about is the $^1S_0 \rightarrow {}^1P_1$. It's lifetime of 5 ns produces a corresponding linewidth of $\Gamma = 2\pi \times 30.5$ MHz and it occurs at 461 nm. This transition is utilized during the Zeeman slowing and first MOT stage. Since the wavelength falls in the blue region of the visible spectrum, this stage of cooling strontium is called the blue MOT in most literature. The Doppler temperature (Eq 2.1), for this transition produces a lower limit of cooling at approximately 1 mK.

There is a small chance, (1:50,000), that excited atoms in the $^1P_1$ state decay into the $^3P_2$ states instead of the ground state. Since the $^3P_2$ state is considered metastable in that the lifetime is much longer than the $^1S_0 \rightarrow {}^1P_1$ transition, and thus will not decay back to the ground state for some time. It is necessary to re-

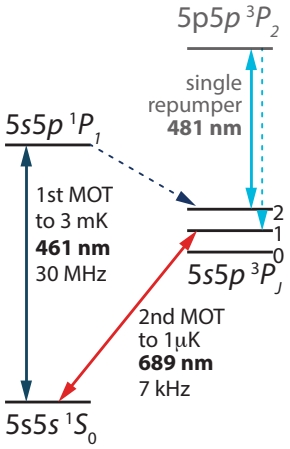

Figure 3.1: Selection of strontium energy levels. Relative energy levels to the $5s5s^1S_0$ can be found in [16]. Not shown is the sub-millihertz clock transition ($5s5s^1S_0 \rightarrow 5s5p^3P_0$).

pump these atoms from the $5s5p^3P_2$ state into the $5p5p^3P_2$ state which will decay into the $5s5p^3P_1$ and eventually back to the ground state.

The $^1S_0 \rightarrow {}^3P_1$ transition happens to be a narrower linewidth than the 461 nm transition at $\Gamma = 2\pi \times 7.4$ kHz and occurs at 689 nm. From the blue MOT, atoms are loaded into this red MOT which has a significantly lower Doppler temperature near 1 μK. Unfortunately, the trapping velocity in the red MOT is too low to efficiently trap the strontium atoms after the Zeeman slower. Working in combination, the blue MOT traps and cools the strontium after the Zeeman slower then transfers the mK atoms to a red MOT. Reaching quantum degeneracy can be achieved through a final stage of evaporative cooling using a far off resonant optical dipole trap. In this work, there is no need for quantum degeneracy and thus the blue and red MOT stages reach cold enough temperatures.

The last important transition for this work is not pictured since it is not used in atom cooling. The benefit to using strontium in matter-wave interferometry on nanophotonics is its ultra narrow, $^1S_0 \rightarrow {}^3P_0$ transition with $\Gamma = 2\pi \times 1$ mHz, 'clock' transition. This transition can be used for high resolution spectroscopic measurements such as measuring the Casimir-Polder force described in section 5.1.

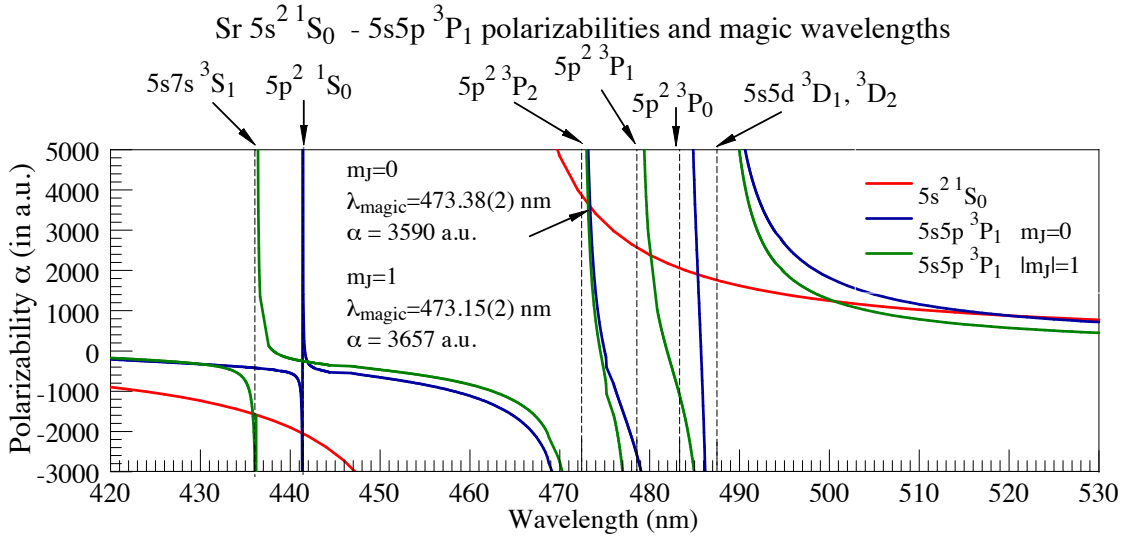

Figure 3.2: Atomic polarizabilities of strontium's $^1S_0$ and $^3P_1$ states. The two wavelengths we propose using are 436 nm and 473 nm wavelengths for the repulsive and attractive FORTs.

Far Off Resonant Trapping

After the blue and red MOT stages, it is possible to tune the distance of the atoms from the nanophotonic chip using far off resonant traps. Light emanating from the photonic structure will have a maximum intensity near the surface and attenuate farther away. The de-tuning dependent force in Eq 2.5 defines the attractive and repulsive nature as well as the magnitude based on intensity. In reality, however, strontium is not a two level system and we need to take into account all atomic transitions when considering the forces that will play a part (Eq 2.6). Since the trap is to be loaded from the red MOT, it is beneficial to cancel the AC Stark shift for the $^1S_0$ and $^3P_1$ states with magic wavelengths where the atomic polarizability is equal for each state.

The wavelength dependent polarizability for the $^1S_0$ and $^3P_1$ states is plotted in Figure 3.2. The 436 nm and 473 nm crossings indicate wavelengths that will cancel the AC Stark shifts of each state. We propose using these wavelengths to trap strontium on nanophotonic structures.

Chapter 4

Apparatus

The main contribution of this work have been the design and construction of an ultra-high vacuum (UHV) apparatus capable of quickly loading photonic chips and trapping strontium. The necessity for such low pressures arises from statistical mechanics. At the micro Kelvin temperatures we are attempting to produce with strontium, any interaction with hotter atoms will transfer energy and limit the cooling process. UHV pressures on the order of 1×10^{-11} or 1×10^{-10} Torr give a mean free path of a particle to be hundreds to thousands of kilometers. By definition of the mean free path, this implies a remaining particle in the chamber will collide with the chamber walls many times before colliding with another atom and the transfer of energy to the cold atoms is minimized.

The main source of residual gasses come from leaks, virtual leaks, or out-gassing. Leaks, as the name implies, occur at poorly secured junctions or at complex parts like valves and windows. Virtual leaks occur when a small pocket of trapped gasses fails to pump and slowly releases the gasses even after UHV pressures are reached. Lastly, out-gassing is an inherent property in all materials similar to virtual leaks. Gasses in the material escape slowly over time. The purpose of using stainless steel is that Hydrogen is the largest out-gassing component and can be easily pumped using highly reactive non evaporable getters (NEGs). Additionally, in the event that Hydrogen is not pumped by the NEGs, the H_2 molecules carry relatively low kinetic energy due to their small mass, and thus will not heat the cold atoms as much as heavier molecules.

Until now, the constraints discussed above relate to the physical necessity of the vacuum chamber. Furthermore, we added two additional constraints in that the chamber should be compact and modular; able to load and trap relatively quickly. Lastly, the apparatus was designed to be structurally sound in order to accommodate our move between laboratories as well as testing for quantum sensor design. Given these choices, we settled on a design incorporated three distinct sections; the strontium oven, the main chamber, and the load lock.

4.1 Strontium Oven

The strontium oven can be considered a source for the experiment. Here, the strontium is heated to vaporizing temperatures and directed in small micro tubules toward the main chamber. Zeeman magnets line the axial tubing and a window at the far end of the system is utilized by the Zeeman laser. In Figure 4.1, the strontium oven is angled upwards and connects to the main chamber through small 5mm tube. The optics on top of the oven, in addition to the Zeeman slower, allow two, 2 dimensional MOT beams to cool and compress the atomic beam. The second 2D mot is off axis from the Zeeman slower, but inline with the 5mm tube connecting the oven with the main chamber. The combination of the Zeeman slower and 2D MOT, help the atomic beam reach velocities below the trapping velocity of the blue MOT. This entire section is purchased from a commercial, atomic source design company known as AOSense. Typical Zeeman slowers are closer to 1m in length and need a substantially larger housing apparatus. The compactness of the AOSense to fit within a 6L volume is far more ideal.

4.2 Main Chamber

The magic happens, or will happen, in the main chamber of the apparatus. Here, the strontium and photonic chips will be married in a fruitful wedding of experimental physics and engineering. Reaching UHV pressures in the main chamber was the first step towards this ideal future. The methods and procedures

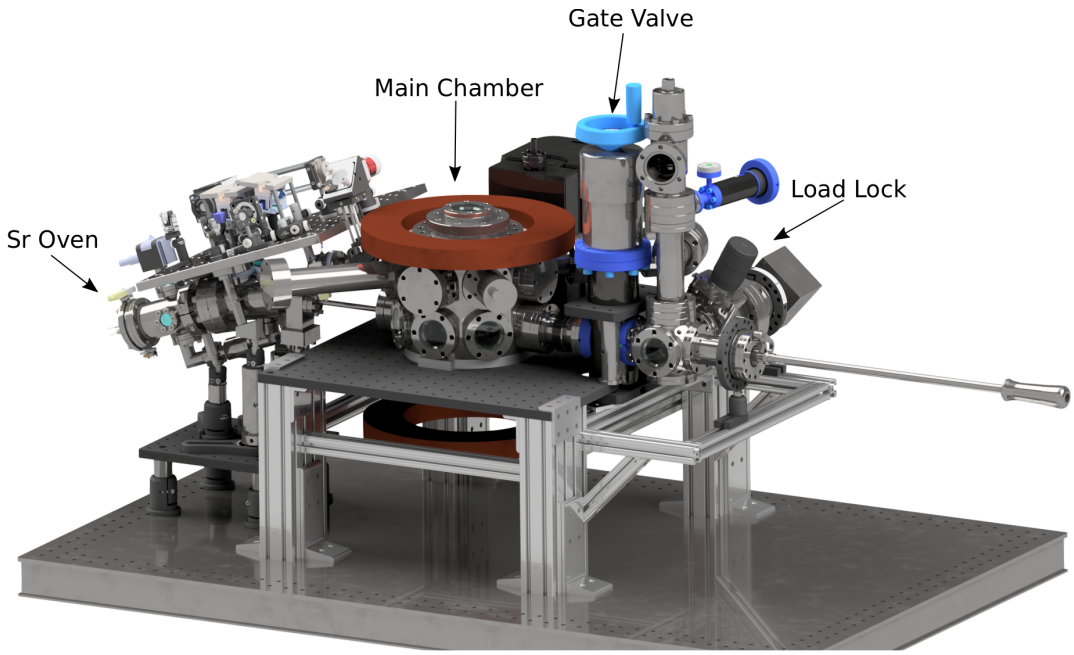

Figure 4.1: 3D rendering of the experiment. The strontium oven, Zeeman slower, and 2D MOT optics are on the left hand side. The main chamber with the 3D MOT coils is in the center and the load lock is on the right hand side.

followed here were also performed during construction of the load lock.

Parts

The chamber itself is an 8" double octagon from Kimball Physics connected to a vast number of standard vacuum components (tees, nipples, canonical reducers, etc) mostly from the Kurt J. Lesker company. Due to space constraints in the load lock section, we had to use close couplers which are extremely difficult to install and even harder to find screws for. 'The Great Screw Debacle of 2018' occurred during my first month of construction when I realized the close couplers were designed in America while the main gate valve was purchased in Europe. Not only that, but the close couplers were specifically designed for a certain screw head, only found on imperial screws. In a classic case of international engineering politics, I negotiated my way to a mediated agreement, though not without a few weeks of frantic screw searching.

Table 4.1: Non standard vacuum parts used in the apparatus.

Description	Company	Part Number
8” main vacuum chamber	Kimball Physics	MCF600-DblSphOct-F2C16
2.75” × .7” close coupler	Kimball Physics	MCF275-ClsCplr-C2-700
2.75” × 1.4” close coupler	Kimball Physics	MCF275-ClsCplr-C2-1400
2.75” optical viewports, fused silica, anti-reflective coating	MPF	A5802-1-CF
6” reentrant optical viewport, fused silica, anti-reflective coating	MPS	Custom
350mm reach wobble stick with flag in line toggle	UHV Design	WS40-350-FT
Series 010 mini UHV gate valve	VAT	01032-CE01
Series 481 main UHV gate valve	VAT	48132-CE01
Series 590 variable leak valve	VAT	59024-GE01
Series 541 right angle valve	VAT	54132-GE02
45 l/s ion pump	Gamma Vacuum	45S-CV-2V-SC-N-N
5 l/s ion pump : 200 l/s NEG combo	Gamma Vacuum	5N-DI-2V-SC-N-N2
200 l/s NEG	Gamma Vacuum	N200
300 l/s NEG	Gamma Vacuum	N300

In addition to the standard parts purchased from Kimball physics and the Kurt J. Lesker company, we had a number of specialized parts as well (see Table 4.1. Separating the load lock section from the main chamber uses a VAT Series 481 All-metal gate valve with a leak rate of 1e-10 Torr L/s. This allows opening the load lock section to atmosphere while keeping the main chamber at UHV in order to load the photonic chips. We also employ a Mini UHV gate valve from VAT to isolate the ion pump and non-evaporable getter (NEG) when venting the load lock section. VAT right angle valves are found on the main chamber and the load lock section to allow independent connections to turbo molecular pumps during pump down of either section. The wobble stick is magnetically stabilized with 350mm of travel. The end of the wobble stick has a flag in line toggle for holding sample holders purchased from Ferrovac.

The main chamber also has 3 non-evaporable getters (NEGs) and a 45L/s ion pump both from Gamma Vacuum. Two of the NEGs have a pumping speed of 300L/s and the third has a pumping speed of 200L/s. Unfortunately, during the NEG activation, the heater element burned out in one of the 300L/s NEGs. It was returned to Gamma for reconstruction, which has taken approximately 2.5 months to fix. Therefore, we temporarily replaced the third NEG with a blank and are only using 2 NEGs as of right now. In the load lock, we installed a NEG/ion pump combination from Gamma Vacuum. The NEG is equivalent to the 200L/s NEG on the main chamber and the ion pump has a 5L/s pumping speed.

We also installed a number of optical viewports for the MOT beams and imaging beams. Since both the blue and red MOT stages need 6 view ports (2 per each axis), the red and blue MOT optics were designed to share windows. The windows were purchased from MPF with anti reflection coating from 400 nm to 700 nm. Four of the MOT viewports are on the lower layer of the main chamber at the locations depicted in Figure 4.2 while the remaining two are vertical (show into and out of the page in Figure 4.2). The viewport on the underside of the chamber is a re-entrant window, inserted into the chamber .75 inches. Future work requires an objective lens in order to image individual atoms. Additionally, the objective lens will be used to focus the laser towards grated fiber couplings on nanophotonic

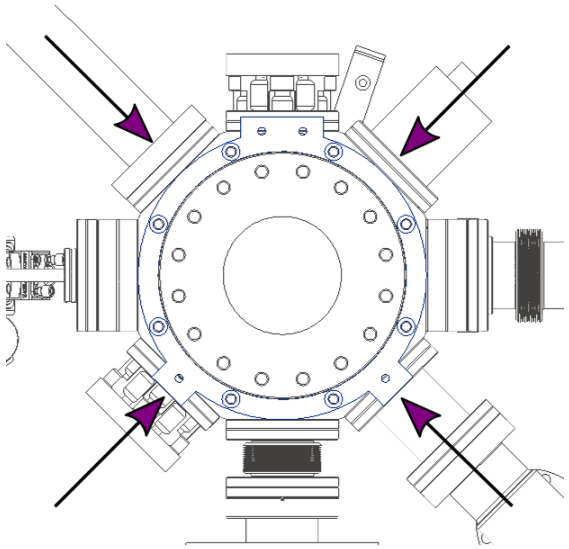

Figure 4.2: Locations of the optical viewports for the blue and red MOT beams in the horizontal plane. An additional pair of beams is going into and out of the paper. The atomic beam approaches from the left while the chip loading is on the right.

chips circumventing the need for in vacuum fiber optics. The specifications of the objective require precise vacuum and air distances for the beam to travel before focusing on the grating couplers, thus, we needed a re-entrant window to meet these needs.

Custom parts were also designed for the interior of the chamber in order to hold the chips close to the atomic beam. The chip holder, Figure 4.3, is a custom steel plate that uses Kimball groove grabbers to mount inside the chamber and Ferrovac SHOM holders to lock the chip in place. It was manufactured at Protolabs and had to be iteratively machined in the Physics machine shop. All custom parts were manufactured out of 304 stainless steel to comply with the rest of the standard vacuum chamber parts.

Cleaning

Despite the care in packaging and shipping vacuum parts, contaminants easily deposit on the stainless steel during the process. Before constructing the

Figure 4.3: Custom chip mount. The Kimball groove grabbers on either end hold the mount inside the main chamber

chamber, every part was cleaned with the following procedure.

1. Sonicate the part in a distilled water and alconox solution at 60° C for 25 minutes.
2. Rinse the part with distilled water over a sink.
3. Let the water-alconox solution cool.
4. Submerge the part in a beaker of methanol.
5. Cover the beaker with plastic wrap and poke holes to allow methanol fumes to escape.
6. Place the beaker in the cooled water-alconox solution.
7. Sonicate for 15 minutes.

8. Drain the methanol and remove the part. Wrap in UHV foil.

Multiple parts were cleaned at the same time in a single beaker with extra care so the knife edges were not damaged. Even after the sonication, additional cleaning of the knife edges with methanol, using lens tissue or something similar, was performed once more when constructing the chamber. There are a number of parts that should not be cleaned, including bellows and gaskets as well as many specialized parts like the wobble stick, valves, and optical or electrical feedthroughs.

Ideally, the custom parts used in the chamber should be produced at a clean room specification, but due to cost and time, they were manufactured at Protolabs and in the Physics machine shop. A substantial amount of oil is needed when machining and these parts had to be soaked for 5-10 minutes in acetone then wiped with methanol prior to the cleaning procedure described above. This cleaning method was highly effective given we reach pressures of 3.8×10^{-11} Torr with the parts inside the chamber.

Construction

Over the past few decades, iterative development of vacuum chambers has led to a fairly robust method of sealing parts in order to maintain low pressures known as Conflat seals. Each part contains a fin metal ridge, called a knife edge. A thin, copper gasket is placed between the two knife edges and vacuum screws are tightened digging the edges into the copper gasket forming a seal from the external atmosphere.

Throughout the entire construction process, it is crucial to wear latex gloves and not to touch any part that will be inside the vacuum, especially the knife edges. Contamination of any part means re-cleaning it following the method above. Additionally, any defect in a knife edges will surely limit your vacuum pressures.

Conflat flanges come in a variety of sizes including 1.33", 2.75", 4.5", and 6" which are used extensively on this apparatus. Depending on the Conflat size, different number of screws are used to tighten the gasket in the knife edges. 1.33" and 2.75" Conflats have 6 holes while 4.5" flanges have 8 holes and 6" flanges have 16 holes. In order to maintain even torque, the flange screws are tightened, first by

hand, then in a star like pattern (see Figure 4.4). The joints should be tightened evenly and are typically stopped with a paper width of space between the two parts.

There are also a number of copper gaskets of which we used; plain copper, annealed copper, silver plated, and annealed silver plated. The silver plating is important to increase the maximum temperature of the gaskets which is important near places of the chamber that will reach high temperatures like the NEGs, but not necessary in most locations. Since we originally constructed the chamber sans optical viewports and valves, we anticipated a high temperature bake thus installing, almost exclusively, silver plated gaskets. Annealed gaskets are softened through the manufacturing process and are used on fragile components or components with feedthroughs like NEGs, ion gauges, or viewports. The ease of assembly between the plain and annealed copper gaskets is noticeable when assembling the joints and, if given the chance, would only use annealed gaskets in the future. Unfortunately, silver plated annealed copper gaskets are more rarely available in the commercial world and had to be ordered from Vacom in Germany in advance due to the large lead time.

In addition to copper gaskets, screw choice is another important criteria in assembling the chamber. At such high torques, anti-locking lubricant is necessary for each screw used. Unfortunately, oil compounds and vacuum do not mix well and any accidental oil contamination inside the vacuum chamber will hinder the low pressure limits of the chamber. Instead, we used silver plated screws which provided a clean lubricant for the construction at high torques. Screw length will vary significantly depending on the components being joined together. Some parts, like short nipples and close couplers, limit the screw access to the through holes while spacers in between two parts require longer screws. Mixing of the two is dangerous since it is likely to need a screw longer than the space available to put the screw in.

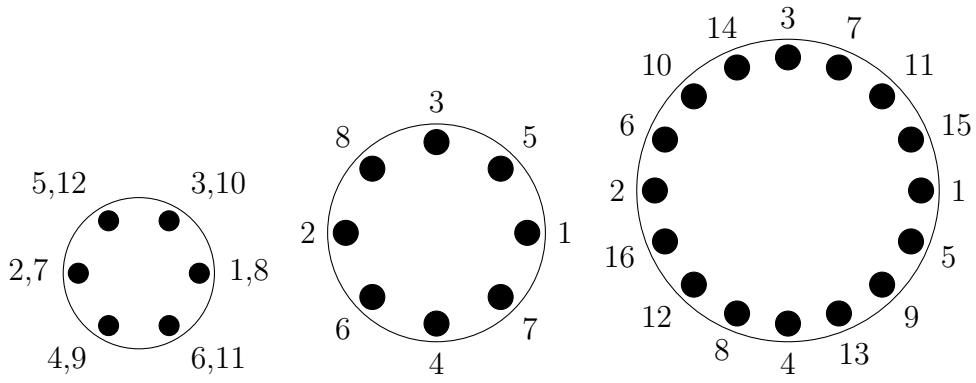

Figure 4.4: Bolt tightening patterns for the different sized flanges. 1.33/2.75, 4.5, and 6 inches from left to right.

Pumping

After the chamber is constructed, we begin pumping through a turbo molecular pump (TMP). TMP's consists of a precisely aligned rotor blade, spinning close to 1000 Hz, followed by a set of stationary blades below. The rotor blade transfers mechanical momentum to the molecules and due to the relative angle between the rotor and stationary blade, molecules are forced into the exhaust. A dry roughing pump connects the exhaust to atmosphere.

A residual gas analyzer (RGA) is used to monitor what gasses remain in the chamber as we pump down. While it is possible to reach UHV pressures with just a TMP, it may take an extremely long time. A large portion of the gasses are due to water condensing on the chamber's inside walls, and slowly evaporating over time; a virtual leak. To remove the residual contaminants more quickly, the chamber is heated an baked at 200C while still connected to the TMP (see Section 4.2).

Once the water peak is no longer decreasing, we cool the chamber and activate the non-evaporable getters (NEGs) and ion pumps. The mechanical nature of the TMP allows it to pump more massive molecules easily while struggling with lighter molecules. Unfortunately, Hydrogen is out-gassed from steel and is not pumped well by the TMP. Instead, the NEGs employ chemisorption and physisorption to pump the residual Hydrogen. The NEGs are activated at temperatures close

to 500C for an hour then, once cooled, the NEG material is reactive to a number of molecules including O_2, H_2, H_2O, CO_2, and N_2. After activation, the NEG will continue to pump these molecules until it becomes saturated. At pressures of 1e-10 Torr, the NEG will reach a saturation of N_2 in 7 years. If a NEG is exposed to atmosphere, it generates a protective coating around the reactive material in a chemical reaction with large quantities of atmospheric gasses. It only needs to be need to be re-activated to begin pumping again.

Finally, the ion pumps are turned on. Ion pumps work through electron bombardment. Encaged in a strong magnet, the ion pump ionizes remaining gas molecules which become attracted to the enshrouding magnet. The ionized molecules are then chemisorbed and physisorbed into an inner surface of the ion pump. In order to maitain UHV pressures, the ion pumps and NEGs remain active until needing replacement.

Bakeout

Baking the chamber by heating it to 200 C (also known as the bakeout), is necessary to speed up the process of reaching UHV pressures in the vacuum chamber. However, the process is not without risk. A common problem during baking vacuum chambers is large thermal gradients across the Conflat seals. Uneven thermal expansion may cause two parts to expand differently affecting the knife edges and, in turn, the gasket seal. Often, the expansion causes a leak. Additionally, the windows cannot exceed a temperature of 180C while most of the valves report a maximum temperature of 250C and should be kept well under these reported values. Naturally, there are also safety concerns with heating a massive, steel apparatus to 200 C.

In order to closely and carefully monitor the chamber temperature, thermocouples are taped using high temperature Kapton tape at a variety of locations on the chamber. These thermocouples, controlled by a beaglebone microcontroller, report the local temperature value of the chamber which is displayed on custom software. Once all thermocouples are placed, a layer of aluminum foil is wrapped around the entire apparatus. To protect the optical viewports from being

scratched, protective mesh coverings are cut and placed over them. The purpose behind this later of foil is that steel is a poor thermal conductor leads to large thermal gradients across the chamber. The foil acts as a better thermal conductor to spread the heat more evenly. Band and ribbon heaters then envelope the foil covered chamber. Finally, we wrap an additional two layers of aluminum foil to keep the heat close to the chamber during the baking process. The entire wrapping process is akin to making a 5-layer dip; thermocouples, foil, heater, foil, foil.

Tape heaters are simple resistors that generate heat when a high voltage is applied, typically from a 120V. Like the thermal gradients, heating too quickly will give rise to rapid thermal expansion, causing shifting of the knife edges and gaskets, or other issues in the more complex gate valves. Most components are designed to withstand a heating rate of 1 C per minute. In order to control the heating rate of the chamber, each heater is connected to a solid state relay (SSR). The SSRs are all controlled though another beaglebone microcontroller which generates a pulse width modulation (PWM), switching the SSR on only for the duration of the PWM width. For example, a 100% PWM will cause the SSR to be always on, essentially the same as plugging the heater into the wall. Alternatively, a 0% PWM means the heater is off. This allows fine control in heating the chamber at a decided rate to a specific temperature.

The heaters are then grouped together (to avoid any of the circuit breaking) and run through emergency kill switches that are controlled by yet another beaglebone. These are emergency use only and can be switched off remotely in case of a problem. In total, the final setup consists of three individual beaglebones, a thermocouple controller, a pwm controller, and a kill switch controller, as well as custom software to monitor the thermocouple readings, the PWM widths of the heaters, and where everything is located on the chamber. The software also monitors the pressure in both the main chamber and load lock as well as an RGA scan to monitor the partial pressures. Finally, an emergency panic script is running which contacts me, or another lab member, in case of a rapid temperature change or an over heated thermocouple. The complete setup is shown in Figure 4.5.

Figure 4.6 shows the partial pressures of pertinent gasses over the time of

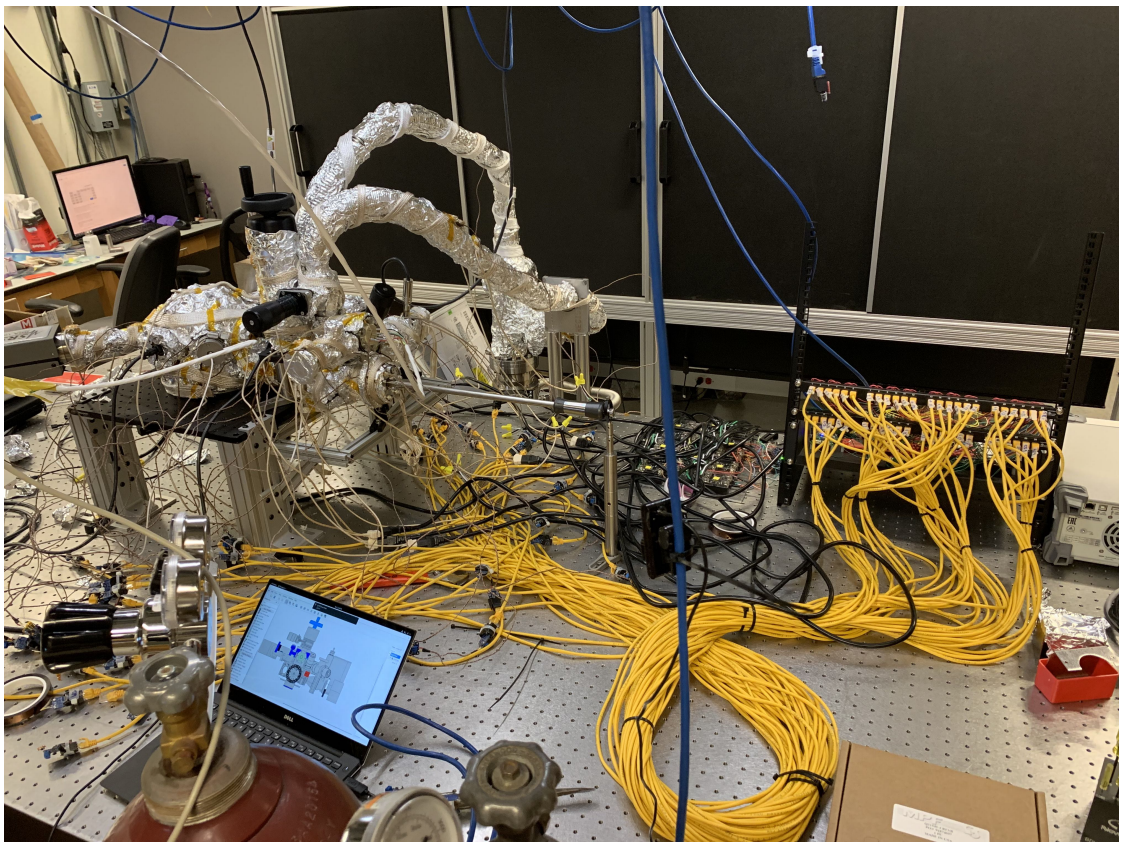

Figure 4.5: Photo of the bakeout setup. The rack contains all three beaglebones as well as the PWM and thermocouple breakouts. The CAT6 cables are each connected to a thermocouple and the heaters are run through the IEC cables. The laptop in the lefthand corner is running the monitoring and control software.

the bake. The first bake was performed on the first constructed chamber (installed with blanks instead of windows). During the first day, temperatures close to 90 C were reached and the NEGs were placed in conditioning mode; set at a temperature around 160 C in order to evaporate any residual water. Over the next 10 days or so, we noticed the partial pressures of components in atmospheric air (Oxygen, Nitrogen, and Argon) were not decreasing. Due to the correlation, we originally had thought it might be caused by the NEG conditioning, but after cooling, I found a large leak in the load lock section near the fourth NEG. Most likely, raising the temperature of this NEG caused thermal expansion in the nearby flanges resulting in a leak.

After tightening the flanges and replacing the blanks with MPF optically coated windows, we resumed baking at the beginning of March. Figure 4.7 plots the partial pressures of a well performed bake with no leaks. We decided to end the bake once the partial pressure of water reached 1e-10 Torr. Before cooling, the ion pumps, RGA, and ion gauges were degassed by applying a higher voltage to quickly evaporate any contaminants remaining on the filaments from the bake. After cooling the system for 24 hours, we activated the NEGs and opened the valve to the AOSense oven reaching a final pressure of 3.8×10^{-11} Torr.

Leak Checking

Leak checking is an important step during the entire process of reaching UHV pressures. The idea is to monitor partial pressure of a specific gas, usually Helium, inside the chamber while spraying the same gas at the Conflat seals outside the chamber. If a leak is detected, the partial pressure of He will rise at a given slope correlated to the leak rate.

The procedure below describes a method of leak checking that can take place as soon as the pressures are below the threshold of the gas analyzer. The SRS 100 gas analyzer can be turned on at pressures starting at 1e-4 Torr.

1. Place the RGA in leak checking mode which will present a graph of He partial pressure vs Time.

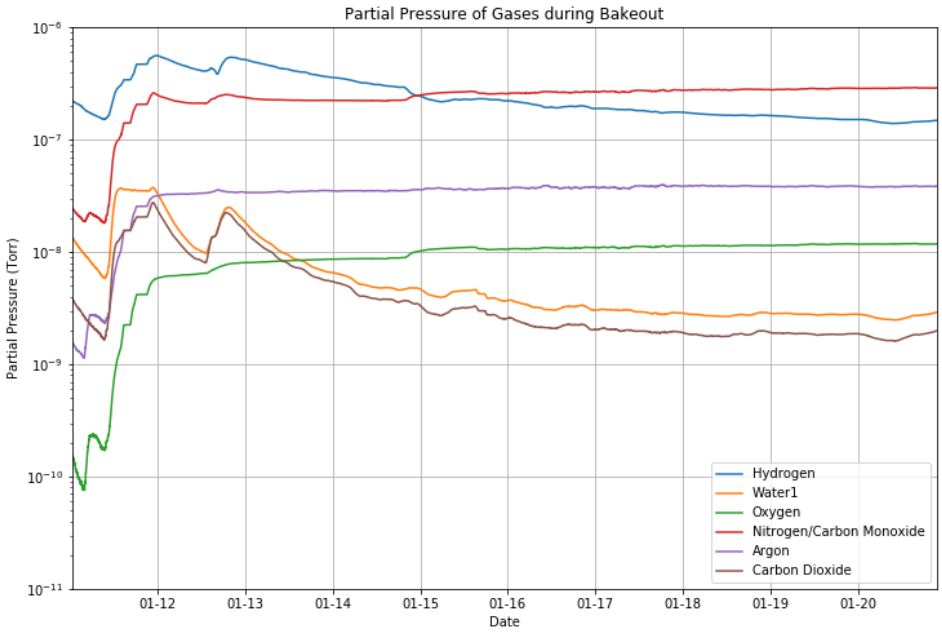

Figure 4.6: Pressure vs time of important gasses during the first bake. The peaks in the beginning were caused by condition the NEGs since they were exposed to atmosphere and were contaminated with a variety of gasses. Unknowingly, a leak was introduced into the system after the NEG conditioning and is distinguishable by the slow rise of Nitrogen, Oxygen, and Argon.

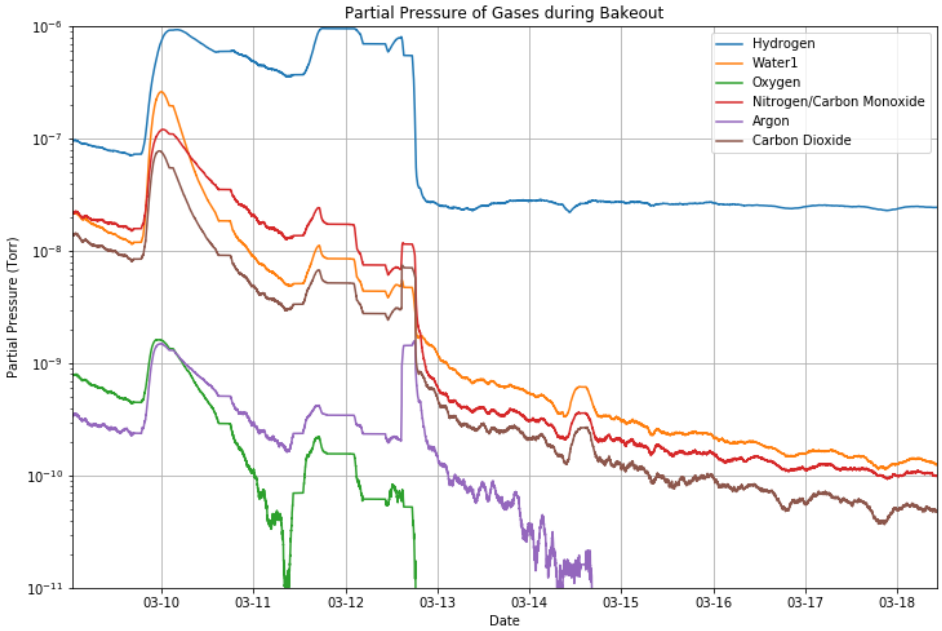

Figure 4.7: Pressure vs time of important gasses during the second bake. Again, we see the NEG conditioning, but this time, all gas pressure decreased as we continued pumping.

2. Record about 5 minutes of a baseline reading making sure the He levels are not too high and do not vary too much inside the chamber.

3. For the chosen Conflat and spray He around the seal. *The flow of He from the canister should be very low, just enough to hear whistling at the end of the tubing.*

4. Wait approximately 1-3 minutes for the He to register at the RGA head. Based on the pumping speed and proximity of the RGA to the pump, a He peak may not be visible despite there being a leak. In this case, close off the pumps and leak checking again.

5. If a leak is present, tighten the Conflat and leak check again. If the problem is not solved, break vacuum, clean the knife edges and replace the gasket.

6. If a leak is not present, move on to the next Conflat seal.

There are more robust methods for leak checking such as purchasing a Helium Leak Checker or inverting the procedure; pumping He into the chamber and monitoring the atmospheric side for any He rise. The method presented here has proven to work in our lab, though the leak checking is more often an art than a science. One substantial benefit in locating where leaks are, is to have enough valves to close off certain sections from the RGA. This will slowly guarantee where leaks are not.

Since the art is dependent on the artist, here are some hints and tips when leak checking a chamber.

- When you're not spraying He on the Conflat seal, stop the flow of He. If the background He levels in the atmosphere are too high and a leak is present, it will be exceedingly difficult to find exactly where the leak is coming from. This is also why the flow should not be too strong.

- Sometimes it is useful to cover the Conflat seal in a plastic bag and fill the bag with He instead of spraying around the seal.

- Compare the leak rate meaured with the specifications of the parts. For example, if a valve or window has a specified leak rate of 1e-9 Torr and you're getting something similar, the part may need to be replaced.

The final step of leak checking for the entire chamber is to perform a rate-of-rise (ROR) test. Depending on when the ROR test is performed, the total pressure rise may not yield a reliable result due to out-gassing from the chamber walls or virtual leaks. Instead, I chose to monitor the partial pressure of Argon which is not out-gassed and is typically pumped out quickly from the TMP due to its large mass, 39 AMU. Argon is roughly .97% of the atmosphere and thus, any Argon rise in the chamber will be from a leak from atmosphere into the chamber.

4.3 Load Lock

The most crucial design element of the apparatus is its ability to load photonic chips to trap strontium on. Atoms on chips are a developed technology for Rubidium atoms, but have yet to be as thoroughly explored with strontium or other alkali earth metals. The load lock section of the chamber enables quick loading of samples and pump down back to 1×10^{-11} Torr within 36-48 hours.

The load lock itself consists of two chambers. The first is where samples are loaded into the wobble stick by removal of a conflat flange. The section also has atmospheric access through a right-angle valve and an additional leak valve for controlled venting of the system. The second section houses the NEG/Ion Pump combination. This part is separated by a VAT UHV Mini gate valve to preserve the lifetime of the NEG. The procedure for loading a new sample are discussed below.

1. Close the mini gate valve to the NEG/Ion Pump section of the load lock. It is crucial not to vent this part of the chamber.

2. Eventually, a blank will be removed exposing the load lock to atmosphere. For larger samples, it may be necessary to open the load lock at the wobble stick, but most likely, the loading can be done by the flange on the side of the cube (Figure 4.8 B). Seal the selected flange in a clean room glove-box or bag.

3. Flood the exterior containment continually with Argon. Fill and empty the containment device multiple times before turning on a continual flow of Argon.

4. Vent the load lock by filtering Argon gas through a sieve. Depending on the experiment, such as the optical nanofibers, it may be necessary to vent through the leak valve to ensure slow pressurizing of the vacuum chamber. If this is not necessary, it is easier to vent through the main right angle valve.

5. Closely monitor the inside pressure of the load lock. Once the load lock is at

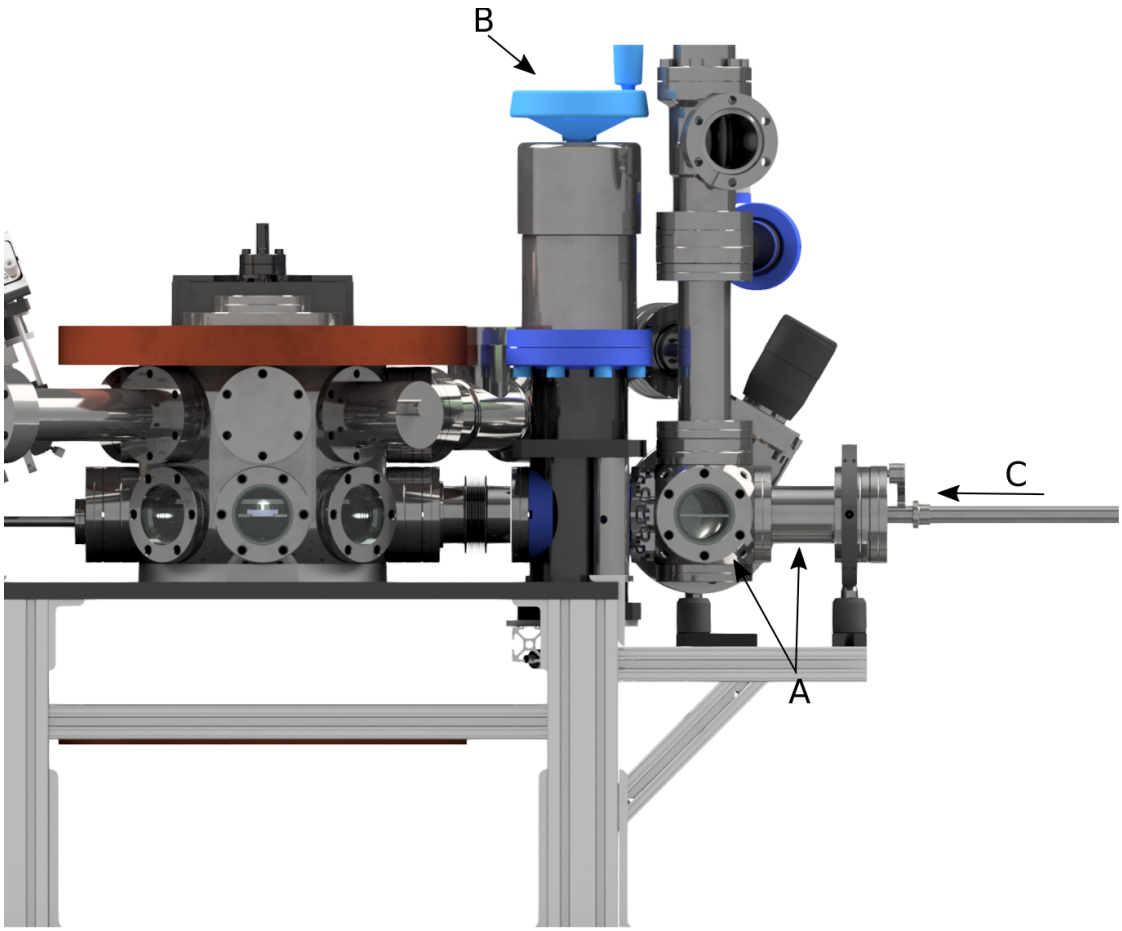

Figure 4.8: Rendering of the load lock section. Points A, B, and C are referenced in the loading procedure.

atmospheric pressure, remove the selected blank and load the chip into the wobble stick.

6. Replace the blank and begin pumping down the load lock section.

7. As the pump down reaches pressures on the the order of 1e-9 Torr, the mini gate valve can be opened to allow the NEG/Ion Pump to help with the pump down.

8. Open the gate valve (Figure 4.8 A) to the main chamber and use the wobble stick (Figure 4.8 C) to transport and lock the sample in the main chamber. The wobble stick is retracted back to the load lock and the main gate valve is closed.

The chip holder in Figure 4.3 and the wobble stick, were designed to work with Ferrovac flag end SHOMs. The wobble stick locks the flag toggle when loading, then unlocks it and retracts once the chip is securely in the mount. One of the proposed experiments involves trapping strontium on a tapered optical fiber. Since the taper must be performed adiabatically, a longer holding plate was necessary. The custom design is modelled on the Ferrovac SHOM design, but is extended in length (Figure 4.9). This also explains why the mount plate is designed with two Ferrovac holders to accommodate the extended sample holder and avoid any unnecessary sagging of the fiber mount.

4.4 MOT Coils

Having achieved UHV vacuum pressure, the project quickly turned to MOT magnets and optics. The MOT uses two magnetic coils in the anti-Helmholtz configuration to achieve a quadropole magnetic field with a linear gradient along each axis. We follow convention by taking the z-axis to be through the axis of the two coils. From radial symmetry of the field and Maxwell's equation $\boldsymbol{\nabla} \cdot B = 0$, we have that $\frac{dB}{dx} = \frac{dB}{dy} = -\frac{1}{2}\frac{dB}{dz}$ and thus, will also form the appropriate magnetic field gradient along the x and y axis. Using the Biot-Savart law, we find the magnetic

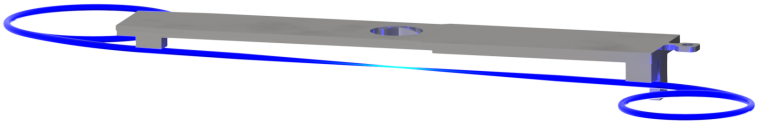

Figure 4.9: Rendering of the tapered optical fiber and custom mounting device. The fiber will be glued to the small pedestals on the chip so the center is aligned with the atomic beam. The center hole allows the vertical MOT beams to trap the atoms on the chip.

field of a single coil with radius r, current I and a number of turns, N, to be

$$B(z) = \frac{\mu_0 N I r^2}{2(z^2 + r^2)^{\frac{3}{2}}}$$

To force the magnetic field to be 0 at $z = 0$, we place two identical coils at $\pm a$ apart with currents $\pm I$. The total magnetic field of both coils is then

$$B_{AH}(z) = \frac{\mu_0 N I r^2}{2((z-a)^2 + r^2)^{\frac{3}{2}}} - \frac{\mu_0 N I r^2}{2((z+a)^2 + r^2)^{\frac{3}{2}}}$$

Deciding on a and r distills down to an optimization problem. In the typical anti-Helmholtz configuration, the desire is to minimize the non-uniformity of the field setting $\frac{\partial^2 B_{AH}}{\partial z^2}|_{z=0} = 0$ which yields $r = 2a$.

Our apparatus has a minimum distance from the atoms, $a = 11$ cm, which equates to $r = 22$ cm; much too large for the chamber. The MOT size, however, is limited by the size of the beam waist, designed to be close to 8mm for both the blue and red MOT. This means we only need to minimize non-uniformity of the field gradient within ± 4 mm from $z = 0$.

Since we could not achieve the anti-Helmholtz condition, we designed the coils to maximize the field gradient for a given atom distance. Solving $\frac{\partial}{\partial r}\frac{\partial B_{AH}}{\partial z}|_{z=0} = 0$ for r gives $r = \sqrt{\frac{2}{3}}a \approx 9$ cm. In reality, the magnetic wire of the coils will have

non-zero width and thus this value is ideally the average radius of the coils. However, because the geometry does not allow smaller coils without separating the coils further, we set this to be the minimum radius.

Further constraints of a field gradient of 50 G/cm and commercial power supplies ranging to 15kW, informed the final design. In order to generate a larger magnetic field gradient, we could increase the number of turns in each coil. However, increasing the number of turns increases the voltage required to generate the same amount of current. Furthermore, adding layers to the coil radially or axially required increased current to generate the same magnetic field gradient since we were farther from the trap center. Ultimately, we decided on 60 turns per coil; 6 axial layers and 10 radial turns per layer. Based on initial calculations and measurement of the coil resistance, running at 280A would produce a field gradient of 50G/cm. The 80m total length of the coils would require a 51V potential across both to reaching about 14.5kW of power from the supply.

Winding

The choice in coil wire was largely influenced by [9, 23]. Using a square, hollow, copper wire in order to water cool through the center of the wire. It was orderd from Small Tube Products with OD of .1875" × .1875" and wall thickness of .035" inches and insulated by S&W wire.

The winding machine for the coils also pays homage to [23, 3] from David Weld's group at UCSB. The frame is built from left-over 80/20 scattered throughout the lab while the remaining parts were purchased from McMaster Carr and machined in house.

The coil holder on which the coils are wound, is designed with a few constraints in mind. First, the amount of force needed to turn the winder should not deform the coil radially. Additionally, the inner radius of the coils should be as close as possible to the calculations above. Even a quarter inch deviation has a large effect on the magnetic field gradient. Lastly, the coil must be constrained axially while the epoxy cures overnight. To account for the first and second issues, a center support of the coil holder made from a 2 inch thick acetol disk is

sandwiched between two aluminum winding plates. In order to control the radius, 3D printed parts are placed along the outside to reach the appropriate thickness. When winding is complete, the coil can easily be removed from the holder without breaking the apparatus.

To hold axial tension in the coils, 3D printed 'clamp blocks' are positioned equally around one side of the coil holder. Screws are inserted into the clamp blocks and tightened during winding to clamp the coil against the far side of the holder. Cotronics NM-25 high temperature, non-magnetic epoxy was used to glue the coils together and the clamps were left in for 24 hours to let the epoxy harden before starting the next layer of winding. The full setup is shown in Figure 4.10

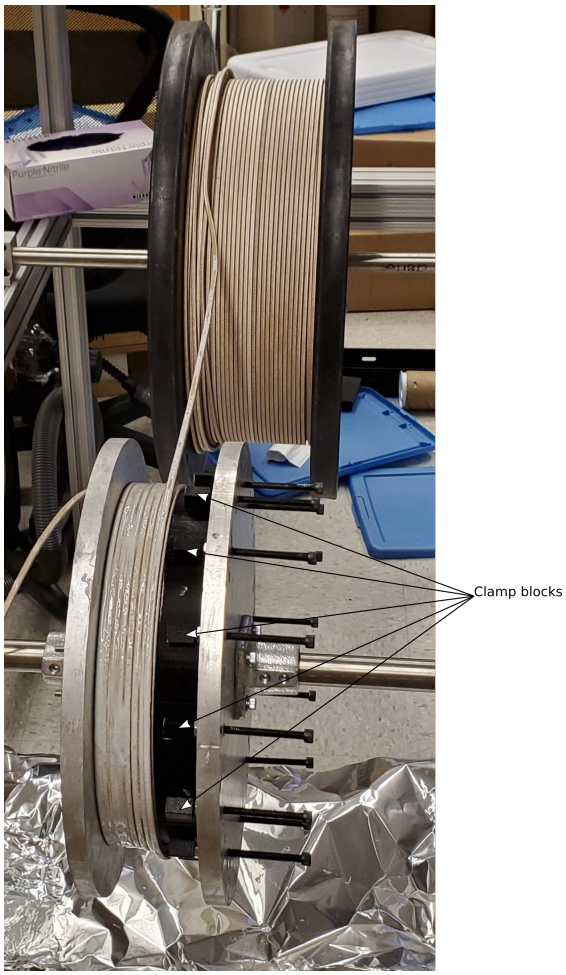

Figure 4.10: MOT coil winding setup. The clamp blocks keep axial tension as the coil is wound.

Cooling

Running 280A through these coils generates significant heating of the copper which is controlled through water cooling. Issues arise when trying to attach circular tubing to square wire. The solution performed by is to solder the square wire inside copper tubing whose ID is equal to the hollow wire's OD which is our current plan and the next step in the apparatus construction. It is necessary to take safety precautions in case the chilled water is not running. Safety interlocks are being designed using thermocouples between each coil layer as well as a flow meter for the water. If water is not flowing or the coils reach too high of temperatures, it will trigger a shutdown of the power supply.

Chapter 5

Future Work

Having reached ultracold vacuum, the next step is to begin focusing on experimental physics. Here, I present two future experiments that are being planned using this apparatus. The first is in collaboration with Dan Steck's group at the University of Oregon and the second with Arno Rauschenbeutel in Vienna.

5.1 Casimir-Polder Force

The Casimir-Polder force is an inherently attractive force that arises from the quantization of the elctromagnetic field. Just as two boats in water are attracted to each other if they are left too close together, the Casimir-Polder force attracts two bodies in the vacuum.

An intuitive derivation of the Casimir-Polder force is given in [30] for a scalar boson field instead of the electromagnetic field. We consider three infinitely conducting plates parallel to each other; two are separated by a distance d and the other two are separated by a distance $L - d$

$$| \leftarrow d \rightarrow | \leftarrow L - d \rightarrow |$$

The modes in the left cavity are

$$k_n(x) = \sin \omega_n x \qquad n = 1, 2...$$

with $\omega_n = \frac{\pi n}{2d}$. Calculating the total vacuum energy results from summing all the modes on the left and the right side. For only the left side, we find

$$\frac{\pi}{2d}\sum_{n=0}^{\infty} n$$

is infinite due to inclusion of arbitrarily high frequency modes. Using regularization, we can correct this by imposing the physical constraint that arbitrarily high energy modes are filtered by the parallel plates. Then

$$\frac{\pi}{2d}\sum_{n=0}^{\infty} n e^{-\frac{an}{d}} = \frac{\pi}{2d}\frac{e^{\frac{a}{d}}}{(e^{\frac{a}{d}}-1)^2}$$

where a is an arbitrary parameter. In the limit that $a \to 0$, we find total energy due to the left hand space is

$$\frac{\pi d}{2a^2} - \frac{\pi}{24d} + \frac{\pi a^2}{480 d^2} + O(\frac{a^4}{d^3})$$

Finally, the force is derived from the energy by varying the distance d and observing the result.

$$\begin{aligned} F &= -\frac{\partial E}{\partial d} = -\frac{\partial}{\partial d}(\frac{\pi d}{2a^2} - \frac{\pi}{24d} + ...) - \frac{\partial}{\partial (L-d)}(\frac{\pi (L-d)}{2a^2} - \frac{\pi}{24(L-d)} + ...) \\ {\scriptstyle a\to 0} &= -\frac{\pi}{24}(\frac{1}{d^2} - \frac{1}{(L-d)^2}) \\ {\scriptstyle L>>d} &= -\frac{\pi}{24 d^2} \end{aligned}$$

We see a significant result. There exists a non-zero vacuum energy producing an attractive force between the two plates and is a direct consequence of the quantization of the field. For the quantization of the electromagnetic field, Casimir found the result to be $\propto \frac{1}{d^3}$. While this method regularizes the high energy modes in between the plates, we can also consider what happens to the low energy modes. Between the plates, the fundamental mode occurs at frequency $\frac{\hbar c}{d}$ while outside the plates, arbitrarily low frequencies can exist. The imbalance between the radiative pressure from the internal and external field modes push the plates together.

An alternative, more thorough method in understanding the Casimir-Polder potential is explored in [13] in which the potential is considered to be an interaction mediated by virtual photons. Considering a spherically symmetric atom near

a parallel conducting plate, the Casimir-Polder potential can be viewed as fluctuations in the atomic dipole as opposed to fluctuations in the vacuum (Figure . The resolution of spectroscopic measurements of dipole fluctuations is often limited by the broad atomic transition linewidth.

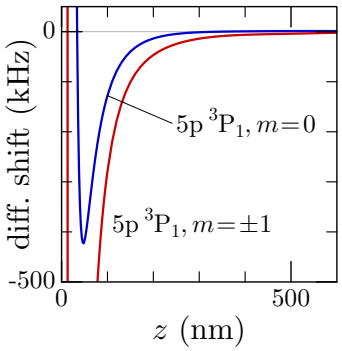

Figure 5.1: Differential level shifts of ^{88}Sr in the $^3P_1$ state as a function of position from the surface.

Previous experiments have been performed to measure the Casimir-Polder force [6], but a reliable spectroscopic method has yet to be shown. Strontium's sub-millihertz clock transition holds promise in being able to detect different level shifts caused by the surface-atom distance. [13] from Dan Steck's lab, proposes using strontium in an optical lattice for fine control of this distance and then performing spectroscopic measurements on the the clock transition.

5.2 Tapered Optical Fibers

Optical nanofibers and ultracold atoms are a strong focus of the atomic physics community. The devices have been used to create optical interfaces between light and matter [28], and probing fundamental atomic physics [21, 14, 15]. As opposed to the typical alkali atoms used in these experiments, once again, strontium's physical properties make it a viable option for further probing of fundamental physics.

Untapered optical fibers have been used in telecommunication and a variety of other applications due to their ability to propagate optical signals with low

loss. This is achieved through a core-cladding design in which each section has a different index of refraction allowing total internal reflection to propagate the light wave through the fiber efficiently. Due to the difference in the index of refraction, a portion of the light leaks out radially from the core into the cladding producing a fairly strong evanescent wave. To counteract this phenomenon, a rather thick cladding is necessary; usually about 10 or 30 times as thick as the core.

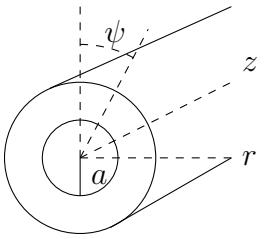

Figure 5.2: Optical fiber schematic (not to scale) with core of radius a. Positions along the fiber are noted in cylindrical coordinates.

Propagation of the light through the core, like all other electromagnetic phenomenon, is governed by Maxwell's equations. Solving these equations given the boundary condition that the fields must be continuous at the core-cladding boundaries, generates a discrete set of possible propagation modes each with its own axial propagation constant defined as β such that $E_z \propto e^{i(\omega t - \beta z)}$. In general, if the core has index of refraction n_1 and the surrounding medium n_2, then the solutions to Maxwell's equations will have two distinct sets; one for $r < a$ and another for $r > a$. This restricts the propagation constant to lie between $n_2 k_0 \leq \beta \leq n_1 k_0$ where k_0 is the vacuum wave vector of the electromagnetic field. Applying boundary conditions at the core-cladding boundary, the details of which can be found in [27, 22], results in an eigenvalue equation for each discrete β

$$\left(\frac{J_l(ha)}{haJ_l} + \frac{K_l'(qa)}{qaK_l(qa)}\right)\left(\frac{n_1^2 J_l'(ha)}{haJ_l(ha)} + \frac{n_2^2 K_l'(qa)}{qaK_l(qa)}\right) = l^2\left[\left(\frac{1}{ha}\right)^2 + \left(\frac{1}{qa}\right)^2\right]^2\left(\frac{\beta}{k_0}\right)^2 \tag{5.1}$$

Here, J_l and K_l are Bessel functions of the first and second kind, a is the radius of the core, and l is an integer value corresponding to the discrete set of propagating modes. The variables

$$h^2 = k^2 - \beta^2$$

$$q^2 = \beta^2 - k^2$$

are introduced depending on whether the mode is propagating in the core (h) or surrounding medium (q) where the former characterizes the rate of oscillation of the mode inside the core as a function of r and the latter is a decay rate in the cladding medium. For example, a larger h corresponds to quicker oscillations in the core while larger q means faster decay and less penetration into the cladding medium [22].

Utilizing the recursive property of Bessel function derivatives, we can rearrange Eq 5.1 to find

$$\frac{J_{l-1}(ha)}{haJ_l(ha)} = \left(\frac{n_1^2 + n_2^2}{2n_1^2}\right)\frac{K_{l-1}(qa) + K_{l+1}(qa)}{2qaK_l(qa)} + \frac{l}{(ha)^2} \pm \left[\left(\frac{n_1^2 - n_2^2}{2n_1^2}\right)^2\left(\frac{K_{l-1}(qa) + K_{l+1}(qa)}{2qaK_l(qa)}\right)^2 + \left(\frac{l\beta}{n_1 k_0}\right)^2\left(\frac{1}{(qa)^2} + \frac{1}{(ha)^2}\right)^2\right]^{\frac{1}{2}} \tag{5.2}$$

The $\pm$ represents two sets of solutions for β; one set corresponds to solutions in which the E_z component is contributes more to the propagation than the H_z component (EH modes) and vice-versa (HE) modes. These equations have no analytical solution and thus must be solved numerically. Since we are interested in modes propagating in the core, the propagation constants will take the form of

$$\beta = \sqrt{n_1^2 k_0^2 - \frac{(ha)_\times}{a}}$$

where $(ha)_\times$ represent intersections of the left and right hand sides. For each integer value of l, there exists a number of crossings which are denoted by m and the modes are named following the convention HE_{lm} or EH_{lm}.

Here we define a new parameter, V, based on normalized values of $\tilde{h} = ha$ and $\tilde{q} = qa$ such that

$$V^2 = (ha)^2 + (qa)^2 = k_0^2 a^2 (n_1^2 - n_2^2)$$

and V is recognized as the well known fiber parameter

$$V = k_0 a\sqrt{(n_1^2 - n_2^2)}$$

The HE_{11} mode can be shown to have the lowest cut-off value while the next propagating mode has a cut-off at $V \approx 2.405$, which can be taken to be the cut-off to transmit a single mode. The necessary fiber radius in order to produce a single mode taper depends on the wavelength in question, k_0. Trapping ultracold atoms on optical nanofibers has been primarily done Rubidium [29, 15] and Cesium [15, 28] which utilize electronic transitions in the 700 and 800 nm range. Unfortunately, strontium's blue transition at 461 nm produces a necessary fiber diameter of ≈ 400 nm. In order to reach such extreme diameters, a precise method for pulling the tapered fibers has been developed in [26]. Here the authors employ a flame pulling technique which induces an adiabatic transition between the multi-mode fiber and the single-mode tapered section transforming the LP_{01} propagating mode into the HE_{11} single fiber mode, and back again, resulting in high transmission through the pulled section.

Like other nanophotonic trapping experiments, we plan to utilize two far off resonant traps on strontium's blue transition. The frequency of these traps is decided by the *magic* wavelengths calculated from the atomic polarizability of strontium following the method in [1]. The red de-tuned magic wavelength is 473 nm while the blue de-tuned magic wavelength is 436 nm. Additionally, the 473 nm will be passed in either side of the fiber generating a optical lattice in the $\pm y$ direction as shown in Figure 5.3. The calculations also include an estimated van der Waal's potential (another version of the Casimir-Polder potential described above) which creates an attractive force for the atoms as the approach the surface of the optical nanofibers. The red and blue de-tuned FORT powers were tuned in order to counteract this attraction and still maintain low power for reasons described below.

Concerns about the fragility of the TOF have been raised and addressed in these calculations. First, high laser power generates a large radiative force which has broken nanofibers in other experiments. To avoid this, the total laser power from both the 436 and 473 nm wavelenghts is kept under 15 mW. Additionally, with regards to loading and pumping with the nanofiber, a number of important changes must be made. To avoid significant air flow disruptions when exposing the

fiber to air, we are designing a laminar flow glove box that will be filled with Argon from which the TOF and mount will be loaded into the chamber. Furthermore, the initial pumping, by turning on the dry roughing pump, produces a significant amount of turbulence which is likely to break the fiber. Counteracting this involves redesigning the load-lock pump down section to utilize the precise, variable leak valve. After pressures on the order of 10^{-2} Torr are reached, a series of valves will be switched to allow pumping on the TMP. Lastly, the glue used to attach the fibers to the mount cannot exceed temperatures of 70 C meaning we will not be able to bake the load-lock after loading the mount. The filling the laminar flow glove box with Argon while simultaneously venting Argon in the interior will help to avoid water and atmospheric gasses from entering the chamber. We have done this previously with a Sigma Aldrich clean room bag with promising results.

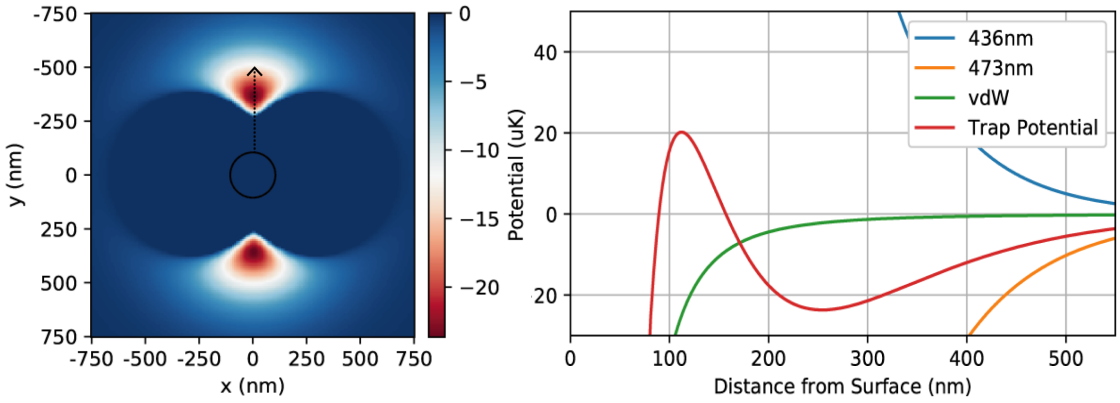

Figure 5.3: Calculated trapping potentials of ^{88}Sr near a tapered optical fiber with a diameter of 230 nm. The red de-tuned laser is at $2 \times .1$ mW power and the blue de-tuned laser is at 2 mW. These parameters give us a trap depth minimum of 24.6 μK at 250 nm from the surface of the fiber.

Chapter 6

Conclusion

In this work, I have presented my proccess in designing and constructing an ultra-high vacuum apparatus for experiments in trapping ultracold strontium over nanophotonic devices. The system reached an ultimate pressure of 3.8×10^{-11} Torr, well within the necessary pressures for ultracold strontium experiments. The combination of a compact AOSense oven, main chamber, and load-lock allow the apparatus to fit within a < 1 m^3 volume. Additionally, the small volume load-lock chamber allows for relatively quick (36-48 hours) loading and unloading to and from the main chamber avoiding the necessary venting and pumping process for the entire system. With the addition of a dry Argon glove box sealed to the load lock, we believe it is possible to decrease this time in the future.

The proposed use of the system is also discussed in the form of two collaborative projects. The first, with Dan Steck at the University of Oregon, involves measuring the Casimir-Polder potential which manifests as adipole fluctuations thanks to strontium's spherically symmetric ground state. We propose trapping strontium in a tightly confined optical lattice in order to control the distance from a dielectric surface. High-resolution clock spectroscopy can be used to observe the CP-induced different level shifts as a function of the distance from the surface.

The second experiment, in collaboration with Arno Rauschenbeutel, involves trapping strontium around a tapered optical nanofiber. I discuss the transition from a multi-mode fiber to a single mode fiber whose radius is determined from the well known V parameter. Two *magic* wavelengths of strontium's $^1S_0$ and

$^3P_1$ states (436 nm and 473 nm), generate the attractive and repulsive dipole forces resulting in a potential minima. The intensity balance between the two controls the distance of the atoms from the nanofiber surface. Additionally, the lesser of the two constrains the maximum fiber radius for a single mode fiber ($\approx$ 210 nm). Using linearly polarized light and passing the 473-nm beam from both sides of the optical nanofiber, we hope to generate a standing wave optical lattice in which strontium atoms will be confined.

This work, and proposed experiments, are the initial steps in developing matter-wave interferometry with strontium over nanophotonic waveguides. Strontium's atomic structure, two-stage MOT cooling and the clock transition, have already been used in high precision measurements. Using these properties in matter-wave interferometry will open new doors to quantum-enhanced metrology.

Appendix A

Quantum Mechanics Overview

To start, we can define two possible states of a stationary atom which form an orthogonal basis for the energies of the system

$$|\alpha\rangle = \begin{bmatrix} 1 \\ 0 \end{bmatrix} \qquad |\beta\rangle = \begin{bmatrix} 0 \\ 1 \end{bmatrix}$$

Energies of the system are expressed as an operator, $\mathbf{H}$, known as the Hamiltonian.

$$\mathbf{H_{atom}} = E_\alpha |\alpha\rangle \langle\alpha| + E_\beta |\beta\rangle \langle\beta| = \begin{bmatrix} E_\alpha & 0 \\ 0 & E_\beta \end{bmatrix}$$

whose expectation value of the energy for state $|\alpha\rangle$ can be denoted as

$$\langle\alpha| \mathbf{H_{atom}} |\alpha\rangle = E_\alpha$$

The atom could also be in a superposition of these two states such that

$$\psi = c_\alpha |\alpha\rangle + c_\beta |\beta\rangle$$

where c_α and c_β represent complex probability amplitudes such that

$$c_\alpha^* c_\alpha + c_\beta^* c_\beta = 1$$

and the probability of finding the atom in the state $|\alpha\rangle$ is denoted as

$$|\langle\alpha|\psi\rangle|^2 = c_\alpha^* c_\alpha$$

Similarly to the expectation value of the energy of state $|\alpha\rangle$, the expectation of the energy of state $|\psi\rangle$ is

$$\langle\psi|\,\mathbf{H_{atom}}\,|\psi\rangle = c_\alpha^* c_\alpha E_\alpha + c_\beta^* c_\beta E_\beta$$

Furthermore, the time evolution of an eigenstate can be found using Schrodinger's equation.

$$\begin{aligned} i\hbar\frac{\partial}{\partial t}\,|\alpha\rangle &= \mathbf{H_{atom}}\,|\alpha\rangle = E_\alpha\,|\alpha\rangle \\ \Rightarrow |\alpha;t\rangle &= e^{-iE_\alpha t}\,|\alpha\rangle \end{aligned}$$

The same differential equation can be solved for an arbitrary state, $|\psi\rangle$ to give a time evolution in terms of the energy eigenstates.

$$|\psi;t\rangle = c_\alpha e^{-iE_\alpha t}\,|\alpha\rangle + c_\beta e^{-iE_\beta t}\,|\beta\rangle$$

This is a pretty boring system given there is no interaction between the states, $|\alpha\rangle$ and $|\beta\rangle$. Another way of saying this is that given the Hamiltonian described above, there is no way to prepare the atom in a state $|\psi\rangle$; the atom will forever live in either state $|\alpha\rangle$ or $|\beta\rangle$. To better model reality, we introduce interactions in the Hamiltonian. Following the 2-level system described above, we define $\mathbf{H_{int}}$ to house the off-diagonal interaction terms.

$$\mathbf{H_{int}} = V_{21}\,|\alpha\rangle\,\langle\beta| + V_{12}\,|\beta\rangle\,\langle\alpha| = \begin{bmatrix} 0 & V_{12} \\ V_{21} & 0 \end{bmatrix}$$

and

$$\mathbf{H_{total}} = \mathbf{H_{atom}} + \mathbf{H_{int}}$$

Appendix B

Atom in a Laser Field

To investigate properties of the atom in a laser field, let's make a change to our atomic Hamiltonian. We want our orthogonal basis to be representative of the electronic structure of the atom and redefine our eigenstates to be $|g\rangle$ and $|e\rangle$ representing the ground and excited states of the atom, respectively. We can arbitrarily set the zero energy to be at the ground-state changing our Hamiltonian as

$$\mathbf{H_{atom}} = \hbar\omega_0 \left|e\right\rangle \left\langle e\right|$$

where $\hbar\omega_0$ is the energy of the excited state relative to the ground state. Additionally, this sets the time evolution of the ground state to be stationary since $E_g = 0 \Rightarrow e^{-iE_g t} = 1$.

The interaction term is then

$$\mathbf{H_{int}} = -\mathbf{d} \cdot \mathbf{E}$$

where $\mathbf{d}$ is the dipole operator, $\mathbf{d} = q\mathbf{r_{electron}}$, and $\mathbf{E}$ is the operator for the electric field which can be written in terms of positive and negative frequencies, $\pm\omega$, field polarization vector, $\hat{\epsilon}$, and the field magnitude, E_0

$$\mathbf{E}(t) = \hat{\epsilon}\frac{E_0}{2}(e^{i\omega t} + e^{-i\omega t}) \tag{B.1}$$

$$= \mathbf{E}^+(t) + \mathbf{E}^-(t) \tag{B.2}$$

In [24], it is shown that the dipole operator can be written in terms of atomic

raising and lowering operators $\sigma := |g\rangle\langle e|$ and $\sigma^\dagger := |e\rangle\langle g|$ as

$$\mathbf{d} = \langle g| \mathbf{d} |\mathbf{e}\rangle \cdot \mathbf{E}(\sigma + \sigma^\dagger)$$

If we evaluate the expectation energy or $\sigma = |g\rangle\langle e|$ in an arbitrary state, $|\psi\rangle = c_g |g\rangle + c_e e^{-i\omega_0 t} |e\rangle$, we find only an unperturbed time evolution dependence in terms of the positive frequency. Likewise, $\langle \sigma^\dagger \rangle \propto e^{i\omega_0 t}$. This allows a decomposition of $\mathbf{d} = \mathbf{d}^+ + \mathbf{d}^-$ and the interaction Hamiltonian becomes

$$\mathbf{H_{int}} = -(\mathbf{d}^+ + \mathbf{d}^-) \cdot (\mathbf{E}^+ + \mathbf{E}^-)$$

The two like terms, $\mathbf{d}^\pm \cdot \mathbf{E}^\pm$ yield an oscillating dependence on $e^{\pm i(\omega+\omega_0)t}$ while the others depend on $e^{\pm i(\omega-\omega_0)t}$. In the rotating-wave approximation, we can take $|\omega - \omega_0| << \omega + \omega_0$ and ignore the like terms and expand out the interaction Hamiltonian to find that

$$\mathbf{H_{int}} = \frac{\hbar}{2}(\Omega\sigma e^{i\omega t} + \Omega^* \sigma^\dagger e^{-i\omega t})$$

and $\Omega = -\frac{\langle g|\hat{\epsilon}\cdot\mathbf{d}|e\rangle E_0}{\hbar}$ is the Rabi frequency.

We can eliminate the time dependence by rotating the entire Hamiltonian into the rotating frame redefining

$$\tilde{\mathbf{H}} = \mathbf{U}\mathbf{H}\mathbf{U}^\dagger + i\hbar(\frac{\partial \mathbf{U}}{\partial t})\mathbf{U}^\dagger$$

where $\mathbf{U}$ is a Unitary operator defined here as

$$\mathbf{U} = \exp(i\omega t \, |e\rangle\langle e|)$$

This produces a new Hamiltonian

$$\tilde{\mathbf{H}} = -\hbar\Delta \, |e\rangle\langle e| + \frac{\hbar}{2}(\Omega\sigma + \Omega^*\sigma^\dagger)$$

where $\Delta := \omega - \omega_0$ is the de-tuning of the laser from resonance of the atomic transition.

Bibliography

[1] M Boyd. High precision spectroscopy of strontium in an optical lattice: Towards a new standard for frequency and time, 2007.

[2] C Foot. *Atomic physics*, volume 7. Oxford University Press, 2005.

[3] Z Geiger. *An Apparatus for Dynamical Quantum Emulation Using Ultracold Lithium*. PhD thesis, ProQuest Dissertations Publishing, 2017.

[4] I Georgescu, S Ashhab, and F Nori. Quantum simulation. *Reviews of Modern Physics*, 86(1):153, 2014.

[5] R Grimm, M Weidemüller, and Y Ovchinnikov. Optical dipole traps for neutral atoms. In *Advances in atomic, molecular, and optical physics*, volume 42, pages 95–170. Elsevier, 2000.

[6] D Harber, J Obrecht, J McGuirk, and E Cornell. Measurement of the casimir-polder force through center-of-mass oscillations of a bose-einstein condensate. *Physical Review A*, 72(3):033610, 2005.

[7] M Jones, C Vale, D Sahagun, B Hall, and E Hinds. Spin coupling between cold atoms and the thermal fluctuations of a metal surface. *Physical review letters*, 91(8):080401, 2003.

[8] M Keil, O Amit, S Zhou, D Groswasser, Y Japha, and R Folman. Fifteen years of cold matter on the atom chip: promise, realizations, and prospects. *Journal of modern optics*, 63(18):1840–1885, 2016.

[9] A Keshet. *A next-generation apparatus for lithium optical lattice experiments*. PhD thesis, Massachusetts Institute of Technology, 2012.

[10] Y Lin, I Teper, C Chin, and V Vuletić. Impact of the casimir-polder potential and johnson noise on bose-einstein condensate stability near surfaces. *Physical Review Letters*, 92(5):050404, 2004.

[11] C Liu, Z Dutton, C Behroozi, and L Hau. Observation of coherent optical information storage in an atomic medium using halted light pulses. *Nature*, 409(6819):490, 2001.

[12] A Ludlow, T Zelevinsky, G Campbell, S Blatt, M Boyd, M de Miranda, M Martin, J Thomsen, S Foreman, and J Ye. Sr lattice clock at $1\times$ 10–16 fractional uncertainty by remote optical evaluation with a ca clock. *Science*, 319(5871):1805–1808, 2008.

[13] P Martin. *Development of a Strontium Magneto-Optical Trap for Probing Casimir–Polder Potentials*. PhD thesis, University of Oregon, 2017.

[14] M Morrissey, K Deasy, Y Wu, S Chakrabarti, and S Nic Chormaic. Tapered optical fibers as tools for probing magneto-optical trap characteristics. *Review of scientific instruments*, 80(5):053102, 2009.

[15] K Nayak, P Melentiev, M Morinaga, F Le Kien, V Balykin, and K Hakuta. Optical nanofiber as an efficient tool for manipulating and probing atomic fluorescence. *Optics express*, 15(9):5431–5438, 2007.

[16] NIST. Energy levels of strontium (Sr I). `https://physics.nist.gov/PhysRefData/Handbook/Tables/strontiumtable5.htm`. Accessed: 2019-06-09.

[17] J Obrecht, R Wild, M Antezza, L Pitaevskii, S Stringari, and E Cornell. Measurement of the temperature dependence of the casimir-polder force. *Physical review letters*, 98(6):063201, 2007.

[18] T Pasquini Jr. *Quantum Reflection of Bose-Einstein Condensates*. PhD thesis, Massachusetts Institute of Technology, 2007.

[19] D Phillips, A Fleischhauer, A Mair, R Walsworth, and M Lukin. Storage of light in atomic vapor. *Physical Review Letters*, 86(5):783, 2001.

[20] S Ritter, C Nölleke, C Hahn, A Reiserer, A Neuzner, M Uphoff, E Mücke, Mand Figueroa, J Bochmann, and G Rempe. An elementary quantum network of single atoms in optical cavities. *Nature*, 484(7393):195, 2012.

[21] G Sagué, E Vetsch, W Alt, D Meschede, and A Rauschenbeutel. Cold-atom physics using ultrathin optical fibers: Light-induced dipole forces and surface interactions. *Physical review letters*, 99(16):163602, 2007.

[22] B Saleh and M Teich. *Fundamentals of photonics*. John Wiley & Sons, 2019.

[23] R Senaratne. *Quantum Simulation of Strongly-Driven Systems Using Ultracold Lithium and Strontium*. PhD thesis, University of California, Santa Barbara, 2018.

[24] D Steck. Quantum and atom optics. *Oregon Center for Optics and Department of Physics, University of Oregon*, 47, 2007.

[25] S Stellmer, F Schreck, and T Killian. Degenerate quantum gases of strontium. In *Annual Review of Cold Atoms and Molecules*, pages 1–80. World Scientific, 2014.

[26] A Stiebeiner, R Garcia-Fernandez, and A Rauschenbeutel. Design and optimization of broadband tapered optical fibers with a nanofiber waist. *Optics express*, 18(22):22677–22685, 2010.

[27] E Vetsch. *Optical interface based on a nanofiber atom-trap*. PhD thesis, Ph. D. thesis, Johannes Gutenberg-Universität Mainz, 2010.

[28] E Vetsch, D Reitz, G Sagué, R Schmidt, S Dawkins, and A Rauschenbeutel. Optical interface created by laser-cooled atoms trapped in the evanescent field surrounding an optical nanofiber. *Physical review letters*, 104(20):203603, 2010.

[29] A Watkins, V Tiwari, J Ward, K Deasy, and S Nic Chormaic. Observation of zeeman shift in the rubidium d 2 line using an optical nanofiber in vapor. In *8th Iberoamerican Optics Meeting and 11th Latin American Meeting on Optics, Lasers, and Applications*, volume 8785, page 87850S. International Society for Optics and Photonics, 2013.

[30] A Zee. *Quantum field theory in a nutshell*, volume 7. Princeton university press, 2010.